

Årgang XCI, Nr. 1, maj 2021

BYGNINGSSTATISKE MEDDELELSER

udgivet af

DANSK SELSKAB FOR BYGNINGSSTATIK

Proceedings of the Danish Society for Structural Science and Engineering

Jacob Nørregaard, Mathias Hagbarth, Pernille L. Andersen, Sandro D. R. Amador, Evangelos I. Katsanos, Rune Brincker:

Estimating the Location and Magnitude of a Point Mass Added to a Steel Structure Using OMA and MVLR1-10

Lars German Hagsten, Jakob Fisker: Capacity assessment of the Örnköldsvik Bridge on the basis of plastic analysis11-19

Bo G Hellers, Håkan Sundquist: A form finding problem – the end supported cantilever beam.....21-45

KØBENHAVN 2021

Eftertryk uden kildeangivelse ikke tilladt
Copyright © 2021 "Dansk Selskab for Bygningsstatik", København
ISSN 1601-6548 (online)

Årgang XCI, Nr. 1, maj 2021

BYGNINGSSTATISKE MEDDELELSER

udgivet af

DANSK SELSKAB FOR BYGNINGSSTATIK

Proceedings of the Danish Society for Structural Science and Engineering

- Jacob Nørregaard, Mathias Hagbarth, Pernille L. Andersen, Sandro D. R. Amador, Evangelos I. Katsanos, Rune Brincker:
Estimating the Location and Magnitude of a Point Mass Added to a Steel Structure Using OMA and MVLR1-10
- Lars German Hagsten, Jakob Fisker: Capacity assessment of the Örnköldsvik Bridge on the basis of plastic analysis11-19
- Bo G Hellers, Håkan Sundquist: A form finding problem – the end supported cantilever beam.....21-45

KØBENHAVN 2021

Redaktionsudvalg

Lars German Hagsten (Redaktør)
Rasmus Ingomar Petersen
Finn Bach
Morten Bo Christiansen
Sven Eilif Svensson
Mogens Peter Nielsen
Linh Cao Hoang
Jakob Fisker

Artikler offentliggjort i Bygningsstatistiske Meddelelser har gennemgået review.
Papers published in the Proceedings of the Danish Society for Structural Science
and Engineering have been reviewed.

Estimating the Location and Magnitude of a Point Mass Added to a Steel Structure Using OMA and MVLR

	Abstract	1
1	Introduction	1
2	Theoretical Background	2
	2.1 Time Domain Poly Reference with Condensation	2
	2.2 Multi Variate Linear Regression	3
3	Structural Model	4
4	Point Mass Scenarios	4
5	Investigation of Predictors for MVLR	5
6	Best Combination of Predictors	7
7	Results	8
8	Conclusions	9
9	References	9

Capacity assessment of the Örnköldsvik Bridge on the basis of plastic analysis

	Abstract	11
1	Introduction	12
2	Characteristics of the Örnköldsvik bridge	12
3	Theory of Plasticity	13
	3.1 Dissipation	13
	3.2 External Work	14
4	Analysis of Failure Mechanisms	14
	4.1 Mechanism 1 (Pure Bending)	14
	4.2 Mechanism 2 (Local Shear)	15
	4.3 Mechanism 3 (Local Shear and Bending)	16
	4.4 Mechanism 4 (Global Shear and Bending)	16
5	Discussion	17
6	Conclusions	18
	References	18

A form finding problem – the end supported cantilever beam

1	Introduction - the problem	21
	1.1 Some general discussion	22
	1.2 General equations for “Euler-Bernoulli Beams”	22
2	Solutions for continuous variation of beam stiffness	22
	2.1 Introduction	22
	2.2 Numerical solution of Eq. (2-5)	23

2.3	The case $n \rightarrow \infty$	27
3	Stepped haunch	29
3.1	Analytical solution for the stepped beam	29
3.2	Numerical solution	37
3.3	Using computer tools to find the largest hogging moment	40
3.4	Obviously	40
3.5	Equilibrium	41
4	Notations	44
5	References	44

Estimating the Location and Magnitude of a Point Mass Added to a Steel Structure Using OMA and MVLR

Jacob Nørregaard¹
Mathias Hagbarth¹
Pernille L. Andersen¹
Sandro D. R. Amador¹
Evangelos I. Katsanos¹
Rune Brincker¹

ABSTRACT

This numerically based study presents a methodology for estimation of magnitude and localization of a point mass added on a small and simple steel structure. This study is linked to the topic Structural Health Monitoring (SHM) aiming to monitor civil engineering structures and detect when a damage has occurred. For this study, a Finite Element (FE) model is used and the damage is simulated by an added point mass. Operational Modal Analysis (OMA) are used to monitor the structure, and Time Domain Poly Reference (TDPR) with condensation are used to identify the modal parameters and mode shapes. Multiple different scenarios with a point mass of different mass magnitude added at different locations of the structure are considered in this study. This scenario based approach and a Multi Variate Linear Regression (MVLR) are used to determine a final model predicting the state of the structure. The results show that the methodology of combining OMA and MVLR can be used for detection of a structural change and return an estimate of the magnitude and location of the point mass with an acceptable accuracy.

1. INTRODUCTION

This article is related to SHM of civil engineering structures. SHM is used to ensure a safely functioning structure throughout its lifetime by detecting when a damage occurs. Damage is indicated by detection of a structural change, for example a change in the stiffness or the mass of the structure. Based on a detected structural change further investigations are carried out to validate the state of the structure and whether a repair is needed. To increase the effectiveness of the investigation the aim is not only to detect that a structural change has occurred, but also get an indication on the location and magnitude of the damage. A reasonably new field in SHM is the use of OMA. An advantage of OMA is that it is an output-only method based on the vibration of the structure, and hereby it is not necessary to know the loading. OMA monitoring operates at operational conditions, which means a continuous monitoring can be performed.

¹ Department of Civil Engineering, Technical University of Denmark

The applicability of OMA for the purpose of SHM has been demonstrated in multiple articles, e.g. [1–3]. These articles demonstrate how an OMA based SHM monitoring system has been used on large civil engineering structures to detect structural changes. In [4, 5] it is furthermore shown how the modal parameters are affected by added mass both to a small steel structure and a 5-story building during the different stages of construction. These articles however do not cover how to determine the magnitude and location of the added mass. The study given in [6] shows how the scenario based approach together with OMA can be used for localization, this study however focuses on load identification and not detection of a structural change. A similar scenario based approach will be used in this study, which means different cases of a point mass added to the structure will be considered. In each scenario, an OMA identification will be performed, and the results obtained will be used to predict the state of the structure.

Based on the articles presented in this section it is shown how an added mass affect the modal parameters of a structure, and furthermore how OMA can be used for localization and magnitude determination on impulse load in a scenario based approach. The scope of this study is to combine OMA and MVLR to determine the location and magnitude of an added point mass. The scenario-based approach used in this study includes multiple mass cases to determine a prediction model based on MVLR. The aim of the MVLR analysis is to obtain a well performing and consistent model predicting the state of the structure. The prediction will be based on outputs of the OMA identification technique. The work presented in this article is based on the master thesis "*Detection of Structural Changes*" [7].

2. THEORETICAL BACKGROUND

Multiple different OMA identification techniques can be used to identify modal parameters, an overview on some of the most common methods are given in [8,9]. For this study, the TDPR [10] with condensation [11] will be used. Furthermore, a brief presentation of MVLR [12] can be found in this section.

2.1. Time Domain Poly Reference with condensation

The original article on TDPR uses the free decays of the structure while for the theory presented below the free decays is represented by the correlation functions as given in [9]. The TDPR is based on the difference equation given in equation (1)

$$\mathbf{y}(n) - \mathbf{A}_1\mathbf{y}(n-1) - \mathbf{A}_2\mathbf{y}(n-2) - \dots - \mathbf{A}_{na}\mathbf{y}(n-na) = 0 \quad (1)$$

where $\mathbf{y}(n)$ is the discrete correlation functions of time lag n , \mathbf{A} contains the Auto Regressive (AR) coefficients and na is the memory of the previous outputs. In equation (1) only the AR coefficients are present due to the assumption of the correlation function acting as a free decay and hereby the Moving Average part vanishes. Stacking the free decays in the $\mathbf{u}_d(n)$ vector and the AR coefficients in the companion matrix \mathbf{A}_c , the following equation can be obtained:

$$\mathbf{A}_c\mathbf{u}_d(n) = \mathbf{u}_d(n+1), \text{ where } \mathbf{A}_c = \begin{bmatrix} 0 & \mathbf{I} & 0 & 0 \\ \vdots & 0 & \ddots & \vdots \\ 0 & \vdots & & \mathbf{I} \\ \mathbf{A}_{na} & \mathbf{A}_{na-1} & \dots & \mathbf{A}_1 \end{bmatrix}, \mathbf{u}_d(n) = \begin{Bmatrix} \mathbf{y}(n-na+1) \\ \vdots \\ \mathbf{y}(n-1) \\ \mathbf{y}(n) \end{Bmatrix} \quad (2)$$

It is assumed that the free decay can be formulated as $\mathbf{y}(n) = \mathbf{b}e^{\lambda n \Delta t}$ where \mathbf{b} is the mode shape, λ is the continuous time pole and Δt is the time increment. From this, \mathbf{u}_d can be rewritten in the following form:

$$\mathbf{u}_d(n) = \begin{Bmatrix} \mathbf{y}(n-na+1) \\ \vdots \\ \mathbf{y}(n-1) \\ \mathbf{y}(n) \end{Bmatrix} = \begin{Bmatrix} \mathbf{b}e^{\lambda(-na+1)\Delta t} \\ \vdots \\ \mathbf{b}e^{\lambda(-1)\Delta t} \\ \mathbf{b} \end{Bmatrix} e^{\lambda n \Delta t} = \boldsymbol{\Phi}_d \mu^n \quad (3)$$

and equation (2) can be expressed as:

$$\mathbf{A}_c \boldsymbol{\varphi}_d = \mu \boldsymbol{\varphi}_d \quad (4)$$

where $\mu = e^{\lambda \Delta t}$. Eigenvalue decomposition of the companion matrix will return the discrete time poles μ and the eigenvectors $\boldsymbol{\varphi}_d$, which is then used to determine the natural frequencies and the mode shapes. In TDPR the first step is to calculate an estimate of the companion matrix, this is done by initially defining a Hankel matrix (\mathbf{H}_1) and a Hankel block row (\mathbf{H}_2) as given below:

$$\mathbf{H}_1 = \begin{bmatrix} \mathbf{y}(1) & \mathbf{y}(2) & \dots & \mathbf{y}(np-na) \\ \mathbf{y}(2) & \mathbf{y}(3) & \dots & \mathbf{y}(np-(na-1)) \\ \vdots & \vdots & \ddots & \vdots \\ \mathbf{y}(na) & \mathbf{y}(na+1) & \dots & \mathbf{y}(np-1) \end{bmatrix} \quad (5)$$

$$\mathbf{H}_2 = [\mathbf{y}(na+1) \quad \mathbf{y}(na+2) \quad \dots \quad \mathbf{y}(np)] \quad (6)$$

where np is the number of discrete points in the free decay. When \mathbf{H}_1 and \mathbf{H}_2 is determined, equation (1) can be rewritten. An estimate of the companion matrix is given in equation (7)

$$\hat{\mathbf{A}} = \mathbf{H}_2 \mathbf{H}_1^+ \quad (7)$$

where the pseudo inverse is denoted by $()^+$ and $\hat{\mathbf{A}}$ is the estimate of the companion matrix. Once $\hat{\mathbf{A}}$ is calculated the eigenvalue decomposition can be performed to determine the frequencies and mode shapes. Before applying TDPR the number of channels is reduced into pseudo channels using condensation. The main assumption of condensation is that the physical modes are more dominant than the noise modes. Based on this assumption the correlation function at time lag zero ($\mathbf{R}(0)$) can be expressed as:

$$\mathbf{R}(0) = \sum_{n=1}^{2N_0} \gamma_n \mathbf{b}_n^T + \sum_{n=2N_0+1}^{2N} \gamma_n \mathbf{b}_n^T \quad (8)$$

where the first sum from $n = 1$ to $2N_0$ represent the physical modes while the second sum from $n = 2N_0 + 1$ to N are the noise modes and γ is the participation vector. Based on the assumption a Singular Value Decomposition can be used to separate the physical modes from the noise modes. To obtain the mode shapes of the structure using the original number of channels the mode shapes determined with condensation must be transformed. Transformation of the mode shapes and a more comprehensive presentation on the theory of condensation is given in [11].

2.2. Multi Variate Linear Regression

The main principles of MVLR are presented in this section. For further information regarding MVLR see [12]. The main equation in MVLR is

$$\mathbf{Y} = \mathbf{Z}\boldsymbol{\beta} + \boldsymbol{\varepsilon} \quad (9)$$

where \mathbf{Y} is the response matrix, the \mathbf{Z} matrix contains the predictors, $\boldsymbol{\beta}$ is the unknown regression coefficient matrix, and the error matrix is denoted as $\boldsymbol{\varepsilon}$. $\boldsymbol{\beta}$ and $\boldsymbol{\varepsilon}$ are unknown, however an approximation of the regression coefficient matrix ($\hat{\boldsymbol{\beta}}$) can be determined by equation (10)

$$\hat{\boldsymbol{\beta}} = (\mathbf{Z}^T \cdot \mathbf{Z})^{-1} \mathbf{Z}^T \cdot \mathbf{Y} \quad (10)$$

The estimated regression coefficients can then be used to predict new responses in $\hat{\mathbf{Y}}_0$.

$$\hat{\mathbf{Y}}_0 = \mathbf{Z}_0 \cdot \hat{\boldsymbol{\beta}} \quad (11)$$

In this study, the $\hat{\beta}$ is determined based on the scenarios included in the simulations. The OMA identified quantities are assembled in the \mathbf{Z}_0 matrix and together with the estimated beta coefficients the state of the structure are revealed in $\hat{\mathbf{Y}}_0$ by equation (11).

3. STRUCTURAL MODEL

The simulations will be carried out based on a FE model of a small steel structure. The structure consists of two parts, a column and a plate attached at the top of the column. The column is a 20 x 20mm SHS profile with a thickness of 2 mm; the remaining dimensions can be seen in Figure 1 a). As illustrated in Figure 1a) the coordinate system is placed centrally in the bottom of the column. The FE model is generated in Ansys where the column is fully fixed in the bottom, and with a fixed connection between the column and the plate. The FE model is meshed with a 20-node solid 3D element with 3 translational degrees of freedom in each node. 134 elements and 666 nodes are used to mesh the model. The weight of the structure is approximately 20 kg and steel with a Young's modulus of 200 GPa is used.

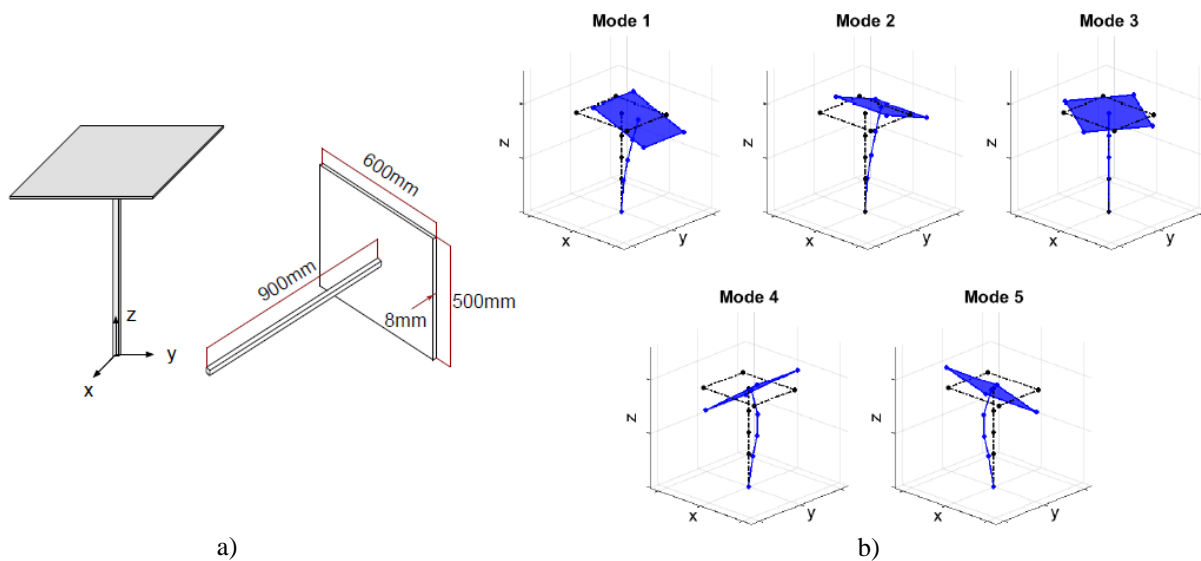


Figure 1: a) Drawing of the structural model b) Mode shapes of the first five modes.

This study only focuses on the first five modes illustrated in Figure 1 b). The natural frequencies have been obtained from the FE software Ansys, and the first five natural frequencies are: 2.812 Hz, 2.847 Hz, 5.965 Hz, 18.184 Hz and 21.588 Hz [7]. The two lowest frequencies correspond to the first bending mode in x and y respectively, the third frequency is the torsional mode and the fourth and fifth frequency are the second bending mode in x and y respectively.

4. POINT MASS SCENARIOS

Due to double symmetry conditions, the point mass will only be applied to the top plate in the first quadrant of the Cartesian coordinate system as illustrated in Figure 2. A 5x5cm grid is made in the xy-plane resulting in 42 different mass locations. A mass position number is assigned to each of the intersections of the gridlines. Only one point mass is added in each scenario and 4 different mass magnitudes are considered which results in 168 different mass cases. The four point mass magnitudes correspond to 2.5%, 5%, 7.5% and 10% of the structural weight. Based on each mass case the corresponding mass and stiffness matrix have been extracted from the FE model and afterwards a response representing a physical measurement is generated in a MATLAB script. For each mass case, 10 responses are generated resulting in 1680 data sets. Following the generated responses, TDPR with condensation is used to identify the modal parameters and the mode shapes for the five modes of interest.

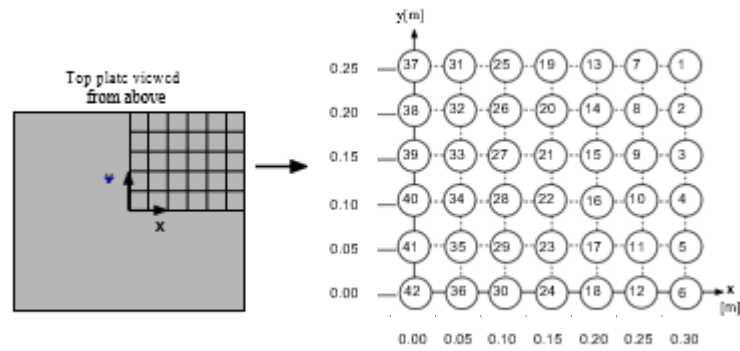


Figure 2: Illustration of the 42 positions where a point mass will be added.

5. INVESTIGATION OF PREDICTORS FOR MVLRL

Utilizing the OMA identification technique the natural frequencies of the first five modes has been determined for all 1680 cases. To show how the frequencies depend on both magnitude and location of the added point mass some of the identified frequencies are presented in the plots below. The plots only include cases where the point mass is added on the x- and y-axis. The graphs show that the frequency of mode 2 and 5 are almost independent on the x-position, Figure 3 a), while the frequency of mode 1 and 4 are almost independent of the y-position, Figure 3 b). The frequency of mode 3 (torsional mode) change equally as a function of distance to the center for both x and y position. For all modes, it should be noted that the frequencies are lower with a higher mass magnitude. Ten markers are found for each scenario corresponding to the 10 responses generated for each mass case at each position. A tendency following a second order polynomial is found for the majority of the modes, and a good agreement is found between identified values and the FE based values illustrated by a solid line.

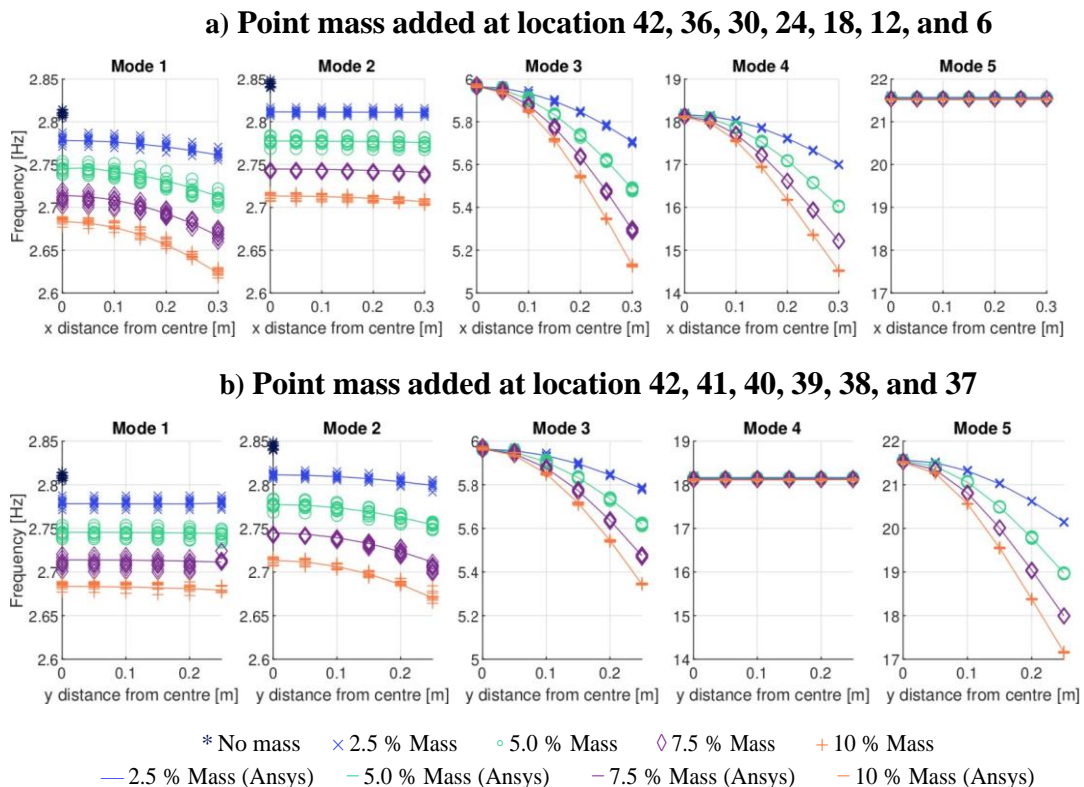


Figure 3: Frequency as a function of the position on the main axis and the magnitude of the point mass. Markers represent the identified frequencies and the line represents the FE obtained frequencies.

In Figure 3, a tendency can be observed, however a discontinuity deviating from this tendency was found when including all 42 mass positions. In Figure 4 a), two 3D plots of the frequency of mode 5 as a function of all 42 mass positions can be seen. For the 3D plot with a mass of 0.5 kg (blue), the frequency follows the tendency of the 2D plots shown in Figure 3. However when the point mass is 2 kg (orange) the discontinuity can be seen in the lower left corner of the 3D plot. This discontinuity was not intended during the design of the model, and further investigation was performed to validate this unexpected behavior of the identified natural frequencies. Investigation of the mode shapes revealed a change in the system, showing that the mode shapes changed from xy-bending modes to modes in the diagonal of the plate. This is illustrated in Figure 4 where the mode shape for the first bending mode when a 2 kg point mass is added has been illustrated. The same phenomenon can be observed in the other bending modes. This phenomenon is important to keep in mind when analyzing and evaluating the performance of the final prediction model. For further information about the discontinuity, the readers may see elsewhere [7].

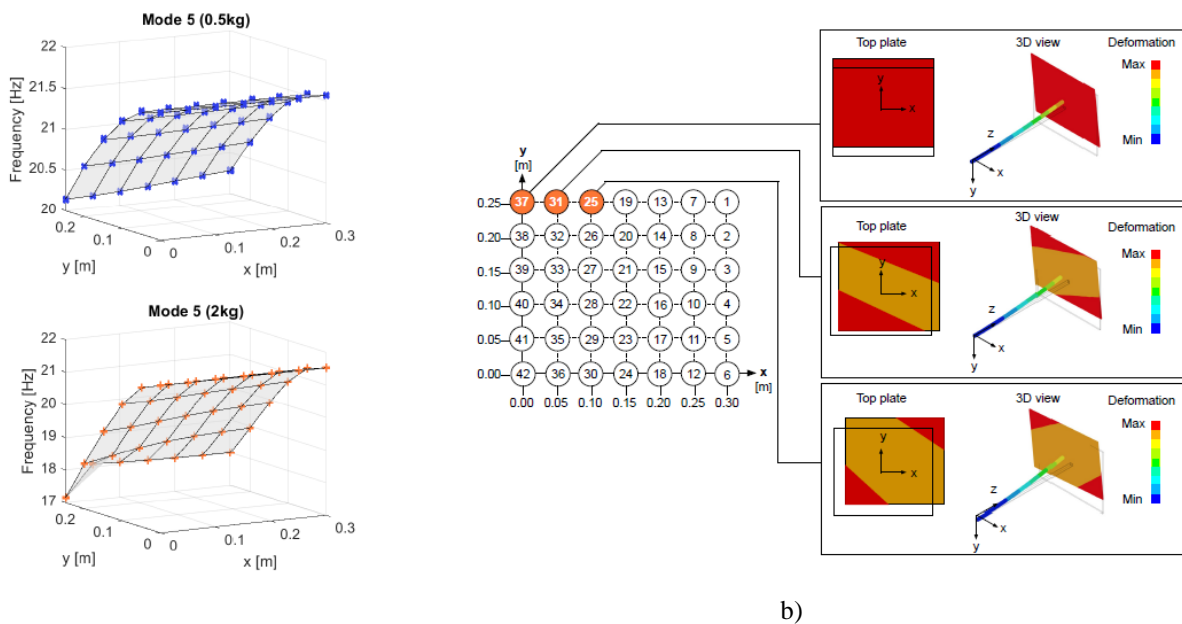


Figure 4: a) 3D plots of frequency for mode 5 in all 168 positions for a 0.5 kg and 2 kg point mass b) Mode shape when a 2 kg point mass is added at position 37, 31, and 25. Mode shapes illustrated how the first bending mode changes towards a diagonal bending mode. Color bar indicate total deformation.

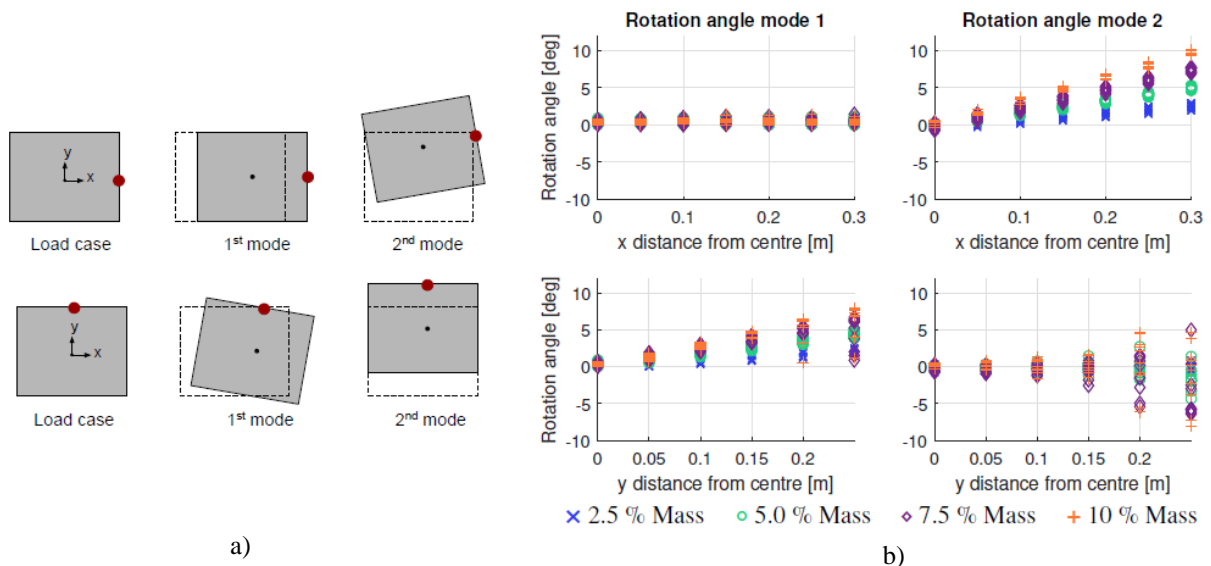


Figure 5: a) Illustration on how the point mass influences the first two mode shapes. • denotes the point mass. b) Angle of rotation as a function of x and y position.

An observation similar to what is presented in [4] shows that a detectable rotation of the top plate dependent on location and magnitude can be extracted from the mode shapes as seen in Figure 5. As illustrated, the x-position provokes a rotation of the second mode and the y-position provokes a rotation of the first mode. A linear dependency between mass, location and angle of rotation was observed as illustrated in Figure 5 b). However, in the scenarios with the discontinuity the rotation angle deviates from the general tendency. The deviation is also a result of modes being closely spaced and modes shifting in some of the scenarios. The Modal Assurance Criterion (MAC) was also considered however the values of the angle of rotation was more consistent which is why it was preferred over the MAC values for the MVLR analysis, this has been further explained in [7].

6. BEST COMBINATION OF PREDICTORS

Multiple different combinations of predictors in the MVLR has been considered in order to determine the best model. Due to computational capacity no more than 16 predictors was included in each of the considered combinations. All possible combinations with three of the groups in Table 1 were considered yielding 35 combinations, which are hereinafter referred to as COPG (Combination of Predictor Groups). Within a COPG all possible predictor combinations have been investigated, e.g. 15 predictors in a COPG $2^{15} = 32.768$ combinations. Analysis showed that the best performing combination for a COPG does not necessarily contain all the predictors. A comprehensive presentation on how the seven groups was selected can be found in [7].

Table 1: Groups of predictors to be used in the MVLR analysis.

Group A	f_1	f_2	f_3	f_4	f_5	
Group B	$\sqrt{f_1}$	$\sqrt{f_2}$	$\sqrt{f_3}$	$\sqrt{f_4}$	$\sqrt{f_5}$	
Group C	f_1^2	f_2^2	f_3^2	f_4^2	f_5^2	
Group D	$f_1 \cdot f_3$	$f_1 \cdot f_4$	$f_2 \cdot f_3$	$f_2 \cdot f_5$	$f_3 \cdot f_4$	$f_3 \cdot f_5$
Group E	$1/f_1$	$1/f_2$	$1/f_3$	$1/f_4$	$1/f_5$	
Group F	$1/f_1^2$	$1/f_2^2$	$1/f_3^2$	$1/f_4^2$	$1/f_5^2$	
Group G	θ_1	θ_2				

To evaluate the performance of each COPG a 10/90 test-training split is performed, where 90% of the 1680 data sets are used to train the model and the remaining 10% are used to test the model. The 10% are randomly selected among the 1680 data sets. The test-training process is repeated 100 times for each of the COPG's and evaluated based on the lowest root mean square error (rmse). Where the rmse is calculated based on the predicted magnitude and location of the mass and the known magnitude and location. The best solution is found for each repetition and might not contain the same predictors in all 100 repetitions for a given COPG. The most frequently occurring best solution is selected for each COPG and used for further analysis and hereby reducing the number of combinations in each COPG to 1 for all 35 COPG's. 100 new repetitions are made on the 35 COPG's based on the same 10/90 test-training data. For each of the 100 repetitions a new $\hat{\beta}$ is determined. Since the aim is to get a single $\hat{\beta}$ usable for detecting all the different scenarios, the scope is to have beta values with a low variance over the 100 repetitions. Furthermore, the beta values of the selected best model must be reasonably low to avoid overfitting. A combination of the rmse and the beta values are used to determine the best model, i.e. the combination of predictors in the final MVLR model. In terms of low rmse many of the COPG's performed equally with an approximate mean rmse of 0.04 for the mass and 0.025 for the xy-position in 100 repetitions. For this analysis, the beta values were inconsistent for the different COPG's. Based on the rmse and beta values the best model has been selected containing the following predictors [7].

$$\mathbf{z}_0 = [1 \quad f_1 \quad f_2 \quad f_4 \quad f_5 \quad f_1^2 \quad f_2^2 \quad f_3^2 \quad f_5^2 \quad f_1 \cdot f_3 \quad f_1 \cdot f_4 \quad f_2 \cdot f_3 \quad f_2 \cdot f_5 \quad f_3 \cdot f_4 \quad f_3 \cdot f_5] \quad (12)$$

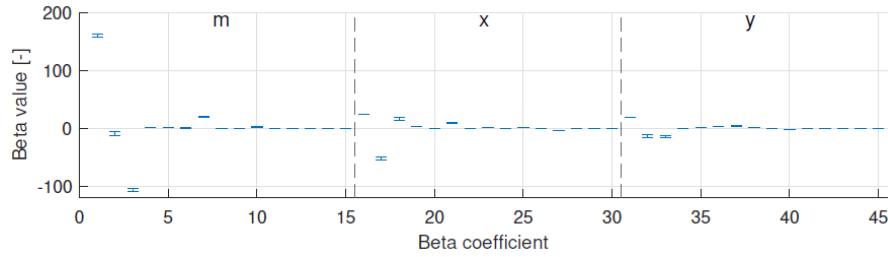


Figure 6: Error bar plot of the beta values obtained in 100 repetitions with the predictors given in \mathbf{z}_0

For this specific model the mean and 99.7% confidence interval of the beta values can be seen in Figure 6, based on the 100 repetitions. The mean of the beta values, with this exact combination, is used to define $\hat{\beta}$. With the established $\hat{\beta}$, the state of the structure can be determined by equation (11) and the OMA identified quantities in \mathbf{z}_0 .

7. RESULTS

Based on the best model a MVLRL is made on all of the simulations, i.e. all of 1680 cases. This gives a \mathbf{Z}_0 of the dimension [1680 x 15] and a response matrix $\hat{\mathbf{Y}}_0$ of dimension [1680 x 3].

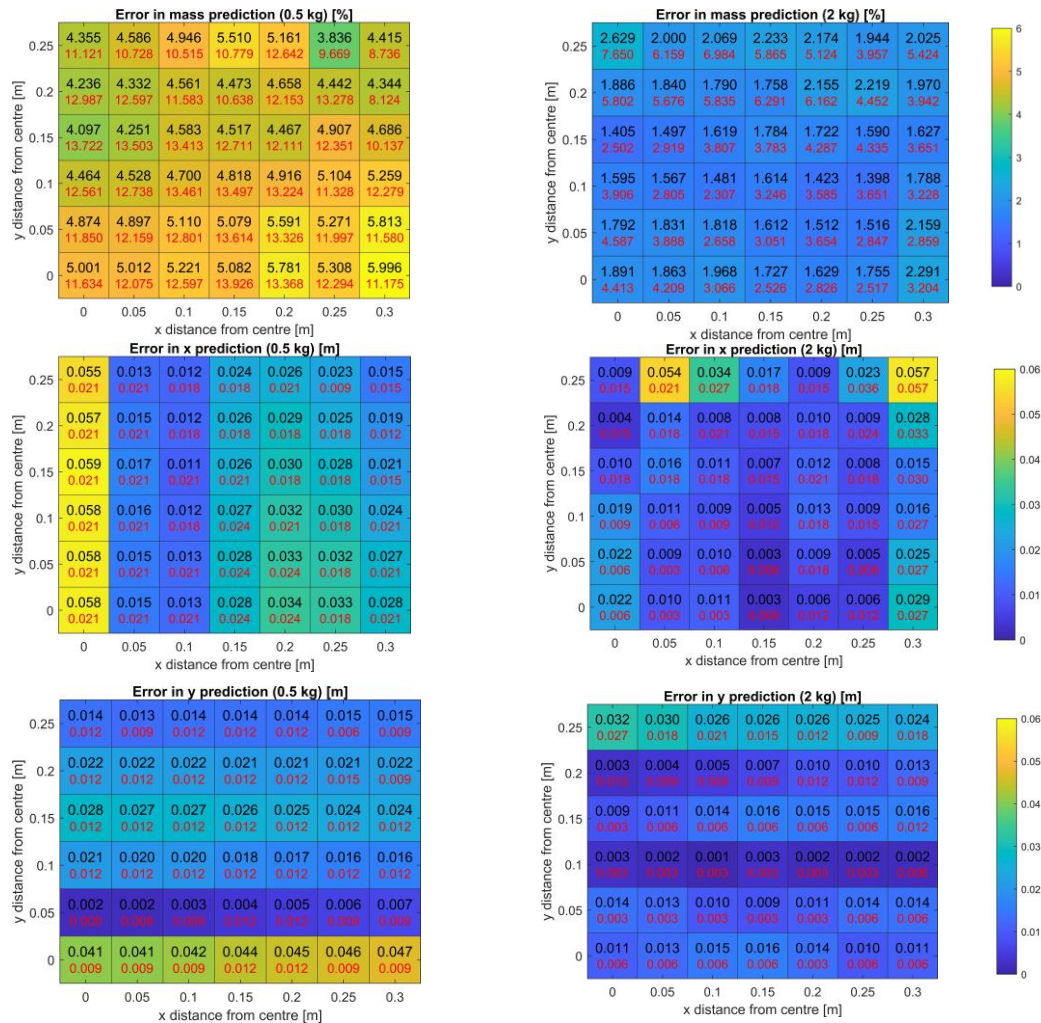


Figure 7: Error in mass and location prediction of a 0.5 kg and 2 kg point mass. Mass error in percentage and location error in m. Color of the squares represent the mean error. Red colored value is the 99.7 % confidence error.

In the figure 7 the mean error in each position is calculated based on the known input values and the predicted values. The black number is the mean error and the red number is the 99.7% confidence error.

Results presented in this article only include the point mass equal to 2.5% and 10% of the structural weight, plots regarding 5% and 7.5% can be seen in [7]. In general, the results show that the mean error of the mass prediction for 0.5 kg is approximately 25 g and the mean error for the 2 kg case is approximately 40 g. Note that for the mass prediction the error and confidence interval is given in percentage.

When predicting the location, the mean error is given in m. For the smallest point mass considered, the prediction has difficulties when the point mass is placed close to the main axis. This is because a small mass does not have a large impact on the frequency when the point mass is placed close to the main axis, as illustrated in Figure 3. Furthermore, it can be seen that the discontinuity affects the prediction, this is especially clear for the x-prediction in the 2 kg case. For the majority of the predictions the mean error is smaller than 0.03 m.

8. CONCLUSION

The present study shines light on how a structural change can be detected based on modal parameters. In this study, it is shown how the output-only OMA based identification technique TDPR with condensation combined with MVLR can be used to predict the state of a structure. Results presented in the previous section prove the potential of this methodology for estimating the magnitude and location of a point mass. The general precision of the estimated mass magnitude and location are within an acceptable range, with a maximum error of 55 g for the mass prediction and a mean error smaller than 0.03 m for the majority of the location predictions. The prediction model presented in this study is not a general model for all structures, however the methodology of the scenario based approach together with OMA and MVLR can be applied to other structures. It is important to highlight that one of the limitations of the scenario-based approach is that the model has only been trained on specific cases limiting the final model. In this study only one point mass is added in each scenario, and the model will therefore not be able to detect if multiple point masses are added. In addition, it is unknown how the model will perform if the point mass magnitude exceeds 2 kg. This study is numerical and based on a simple structure, which means further investigations, including experimental studies, are needed to prove the potential of this methodology for the purpose of SHM.

9. REFERENCES

- [1] Magalhães, F., Cunha, A. and Caetano, E. (2012) Vibration based structural health monitoring of an arch bridge: From automated OMA to damage detection *Mechanical Systems and Signal Processing*, 28, 212-228.
- [2] Amador, S.D.R., Magalhães, F., Cunha, A., Caetano, E. and Martins, N. (2017) Automated modal tracking in a football stadium suspension roof for detection of structural changes *Structural Control and Health Monitoring*, 24.
- [3] Brownjohn, J.M.W., Magalhães, F., Caetano, E. and Cunha, A. (2010) Ambient vibration re-testing and operational modal analysis of the Humber Bridge *Engineering Structures*, 32, 2003-2018.
- [4] Bernagozzi, G., Ventura, C.E., Kaya, Y., Landi, L. and Diotallevi, P.P. (2017) Comparison of OMA techniques and effect of added mass on the modal parameters of a small steel frame *IOMAC 2015*, 24, 10-12.

- [5] Astroza, R., Ebrahimian, H., Conte, J.P., Hutchinson, T.C. and Restrepo, J.I. (2013) Evolution of Dynamic Properties of a 5-Story RC Building During Construction *Topics in Dynamics of Civil Structures, Volume 4. Conference Proceedings of the Society for Experimental Mechanics Series*
- [6] Vigsø, M., Tarpø, M., Hansen, J.B., Brincker, R. and Georgakis, C.T. (2019) Scenario based approach for load identification *Conference Proceedings of the Society for Experimental Mechanics Series*, Springer New York LLC, 117-125
- [7] Hagbarth, M. and Nørregaard, J. (2020) Detection of Structural Changes Master Thesis. Technical University of Denmark (DTU), Kgs. Lyng-by, Denmark
- [8] Magalhães, F. and Cunha, A. (2011) Explaining operational modal analysis with data from an arch bridge *Mechanical Systems and Signal Processing*, 25, 1431-1450
- [9] Ventura, C.E. and Brincker, R. (2015) Introduction to Operational Modal Analysis John Wiley & Sons, 1st ed.
- [10] Vold, H., Kundrat, J., Rocklin, G. and Russell, R. (1982) Explaining operational modal analysis with data from an arch bridge *Mechanical Systems and Signal Processing*, 91, 815-821
- [11] Olsen, P., Juul, M., and Brincker, R. (2019) Condensation of the correlation functions in modal testing *Mechanical Systems and Signal Processing*, 118, 377-387.
- [12] Quick, C. and Kang, J. (2013) Multivariate Multiple Regression with Applications to Powerlifting Data University of Minnesota, Duluth

Capacity assessment of the Örnköldsvik Bridge on the basis of plastic analysis

Lars German Hagsten

Jakob Fisker^{1,2}

Abstract

In 2006 an old concrete railway bridge in Sweden, the Örnköldsvik bridge, was tested to failure on site. The bridge had been decommissioned after some fifty years in service. The tests formed the basis for an extensive research programme concerning capacity assessment of existing concrete bridges, with special focus on the development of numerous advanced finite element models. In this paper the Örnköldsvik bridge is analysed on the basis of the theory of plasticity, and more specifically, the upper bound method or kinematic method. This is achieved by setting up a number of kinematically admissible failure mechanisms and calculating the corresponding load capacity to each of these mechanisms. In the paper four different failure mechanisms of different complexity are analysed. It turns out that the critical mechanism can be described as a combination of bending and shear in different parts of the bridge. The calculated critical capacity is in good agreement with the capacity observed in the test. In addition, the critical mechanism is found to comply with the reported observations. It is illustrated, that the upper bound method not only constitutes a method for determination of the capacity. It is also a method that allows for important aspects of the physical behaviour of the structure as-built to be highlighted, and critical parts of the structure to be identified. The method thereby serves as an important tool, especially, in relation to assessment of existing structures. Furthermore, the upper bound method allows for quick estimates that are useful in combination with more time-consuming finite element based approaches.

1. Introduction

Activities related to conservation of existing concrete bridges constitutes a significant part of daily practice within bridge engineering. This involves assessment of structural integrity and capacity, and, if needed, measures concerning appropriate ways of strengthening. The assessment of existing concrete bridges is a complicated task, that besides inspection of exiting drawings typically also includes an inspection of the as-built conditions and state of deterioration; possibly supplemented by testing for basis material properties of steel and concrete. This requires prior detailed knowledge of the anticipated structural behaviour and the corresponding critical parts in order to focus the attention of on-site inspections on these parts of the structure.

¹ Aarhus University School of Engineering, 8000, Aarhus Denmark

² COWI A/S, 8000 Aarhus, Denmark

Throughout the years invaluable insights in regards to structural behaviour and remaining capacity of existing concrete bridges has been gained through full scale testing of decommissioned concrete bridges, and quite often a substantial gap between predicted capacity and actual capacity, measured on the basis of tests, has been observed. Especially when considering failure modes resembling shear- or punching shear failures, as revealed in a number of works involving testing and assessment of existing bridges, see *e.g.* [1],[2],[3] & [4].

Various strategies have been proposed and implemented in order to deal with this apparent gap between predicted capacity and actual capacity. One approach is the use of proof loading as the basis for load rating and upgrading; especially in cases where original project material is insufficient, and/or the bridge suffers from significant deterioration, see *e.g.* [4][6][7]. As an alternative to proof loading others advocates for procedures involving mainly non-linear FE analysis of gradually increased complexity, see *e.g.* [5]. In line with the “level-of-approximation”-philosophy of the fib model-code, the ambition put forward is to obtain more accurate predictions as the “level of assessment” is increased.

The often observed gap between predicted and actual capacity, can in the review of drawings and static models of existing bridges to a large extent be seen as the result of a discrepancy between the actual structure and assumed static behaviour. It is not a matter of applying more sophisticated models but more a matter of applying (simple) models reflecting the structural behaviour of the design. This paper presents an analysis of a reinforced concrete integral bridge by application of the upper bound theorem of the theory of plasticity. The approach is based on possible failure mechanisms rendering, not only a predicted capacity, but also highlights the physical behaviour and the critical parts of the structure/bridge.

2. Characteristics of the Örnköldsvik bridge

The two-span bridge was tested to failure on-site by the application of mainly concentrated loads. An elevation of the bridge is shown in Figure 1. The concentrated loads were applied at the centre of the left span. The self-weight, including gravel fill-in, was approximately 84 kN/m [3].

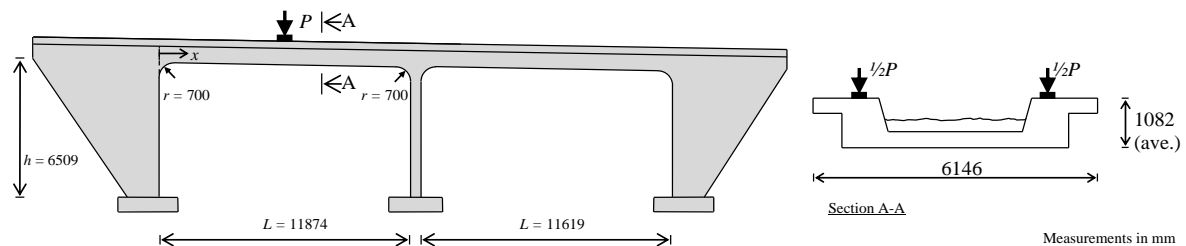


Figure 1. Elevation of the Örnköldsvik bridge. Reinforcement is not shown.

Due to variations of the structural height of the beam-segments near the supports and to varying degree of top- and bottom longitudinal reinforcement the moment capacity varies along the beam-segment. The diagram in Figure 2 illustrates the moment capacity as a function of the distance, x , from the inner face of the left support (origin shown in Figure 1). The moment capacity is calculated on the basis of a constant stress, f_c , in compressive zone. Reinforcement in compression is not taken into account.

Prior to the test, the left span (the loaded span) was strengthened with a total of twenty CFRP bars at the bottom face. For this reason, the positive moment capacity of the left span was significantly greater than the positive moment capacity of the right span. The bridge was slightly curved in plan. However, previous analysis has shown that the influence of the thereby introduced torsion is limited [8] and will be ignored in the following.

The measured average concrete compressive strength was approximately $f_c = 68.5$ MPa, while the yield strength of the reinforcement was $f_y = 441$ MPa ($\text{\O}16$) and $f_y = 411$ MPa ($\text{\O}25$). The strength of the CFRP-strips was $f_{\text{CFRP}} = 2266$ MPa.

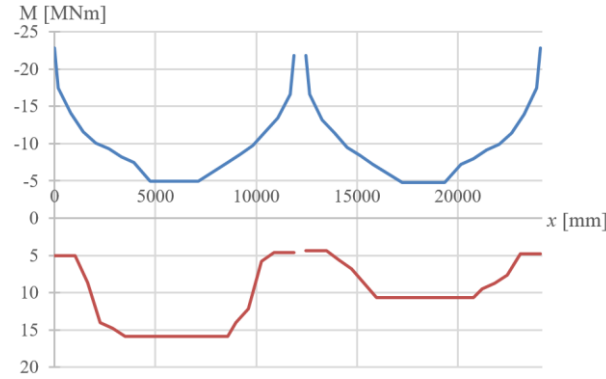


Figure 2. Positive and negative moment capacity as function of the distance from inner face of the left support (see Figure 1)

3. Theory of Plasticity

Upper bound solutions are based on kinematically admissible failure mechanisms, and the load carrying capacity is then determined using the work equation, where the internal work (the dissipation) is equalled with the external work of loads. Material are assumed perfectly plastic, and all displacement increments are assumed localised along certain failure lines or in plastic hinges. The part of the structure in between failure lines or plastic hinges is regarded as rigid.

3.1 Dissipation

For a given failure mechanism and corresponding relative displacement increments, the dissipation per unit area due to sliding along a failure surface in the concrete is evaluated as;

$$W_{i,c} = \frac{1}{2} \cdot \nu f_c \cdot u \cdot (1 - \sin(\alpha)) \quad (1)$$

In (1) u represents the relative displacement increment, while α is the angle between the direction of the relative displacement and the failure surface, see Figure 4. The effective strength of the concrete is evaluated by the introduction by the effectiveness factor taken as;

$$\nu = \max\left(0.7 - \frac{f_c}{200}, 0.45\right) \cdot \nu_s, \quad \nu_s = 0.5 \quad (2)$$

This effectiveness factor includes the classical expression for members reinforced with distributed shear reinforcement. As the structure, and specifically the primary beams, is rather massive, and reinforcement is only placed along the outer edges, a large part of the concrete away from the edges were left with no reinforcement. For this reason, the classical effectiveness factor is multiplied by 0.5 according to works of Nielsen and co-workers [9].

In the specific case of a plastic hinge the dissipation due to an increment rotation is evaluated as;

$$W_{i,c} = \gamma M \quad (3)$$

Here γ is the rotation in the plastic hinges and M is plastic moment capacity of the hinge, see also Figure 3. Reinforcement crossing the failure surface will also provide resistance towards failure.

The reinforcement is assumed to be inactive with respect to compression, and the contribution from the reinforcement is thus evaluated simply as the work done/dissipation during an incremental elongation under the assumption of tensile yielding. Any other resistance offered by the reinforcement is ignored.

3.2 External work

The external work is determined as the product of the incremental downward displacement at the position of the load and the load. The extension of the loading plates is not taken into account when calculating the external work, and the concentrated load is thus assumed to act in a single point. The contribution from distributed load will also be included.

4. Analysis of failure mechanisms

A total of four failure mechanisms (1 to 4) will be presented and analysed. The three first mechanisms only activates the left span, subjected by the concentrated loads, while the 4th mechanism involves a greater part of the bridge.

Mechanism 1 is considered in order to examine the bending capacity of the element in the left span, and only involves rotational displacements, while Mechanism 2 is introduced in order to examine the shear capacity in the region of the concentrated loads. The mechanism violates the geometrical boundary conditions, which leads to the introduction and analysis of Mechanism 3. In this mechanism, a significant part of the dissipation is due to bending at the intermediate support. From considerations of the flexural capacities in the different segments joining at the intermediate support a final mechanism, Mechanism 4, involving a major part of the bridge, is presented and analysed. This later mechanism turns out to be the most critical.

4.1 Mechanism 1 (pure bending)

Mechanism 1, as illustrated in Figure 3, represents a possible failure mechanism characterised by pure bending at three plastic hinges. The mechanism only involves the left (loaded) span.

The load is displaced downwards due to the relative rotation of the two parts on each side of the concentrated load, as they rotate. The two parts have a common point of rotation located under the concentrated load in a distance z from the top side of the element. Near the ends two additional rotational points exists. The location of these points is defined by the horizontal and vertical distance x and y , respectively, from the centre of the circular part of the bottom face of the beam element at the transition to the supports. The resulting compressive force F_{cl} acts in the direction of the tangent of circular segment at the considered section.

In general, the rotation of the two beam parts is controlled by the downward displacement u under the concentrated load which results in the angular rotation, γ , of the two half parts of the span. The three rotational points are not positioned on a straight line, and in order for the mechanism to be geometrically possible there must also be a horizontal movement of the outer rotational point, resulting in a slightly greater rotation of the hinge near the outer support.

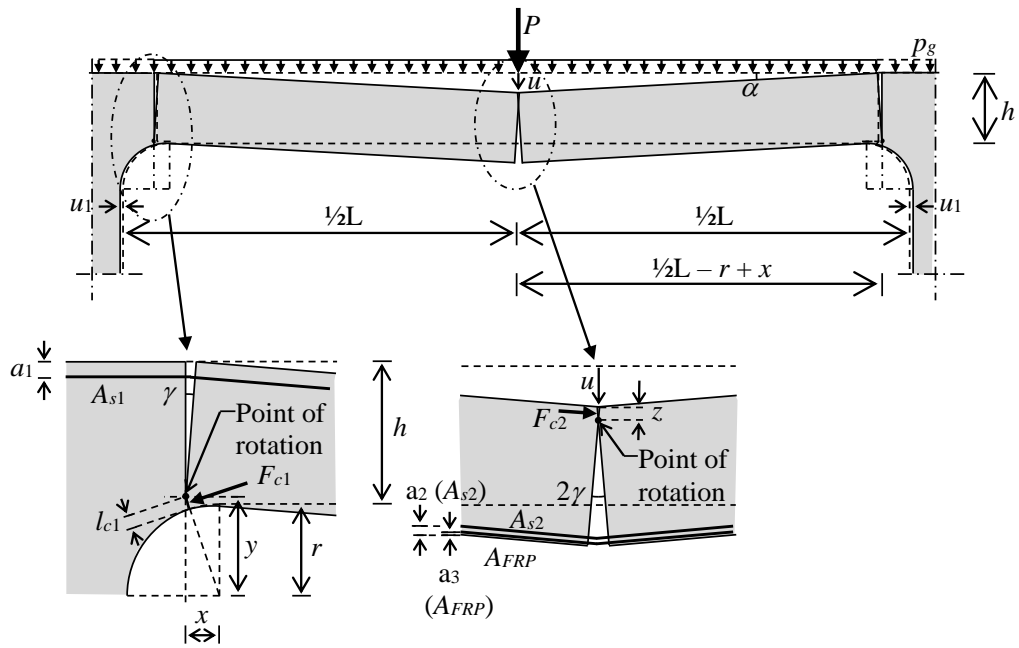


Figure 3. Mechanism 1. Mechanism characterized by pure rotation

Having described the kinematics of the mechanism it is possible to set up the expressions for the internal and external work. The capacity is found by minimisation of P with respect to x , y and z , and the optimizations leads to $P = 13.2$ MN. This is obtained for: $x = 148$ mm, $y = 727$ mm and $z = 73$ mm.

4.2 Mechanism 2 (local shear)

The starting point for the analysis with respect to the shear capacity will be the classic shear mechanism shown in figure 4. The mechanism does not comply with the geometric boundary conditions as the right part is assumed to move downwards by pure translation. This will, however, be taken into account in mechanism 3.

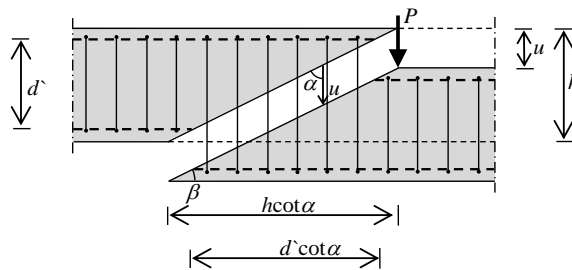


Figure 4. Mechanism 2. Classic shear mechanism

When considering sliding in the concrete the question is how much of the cross-sectional area that will be effective, and therefore should be included. As proper shear reinforcement is only provided in the part designated A_2 (grey shaded), only this part will be considered when assessing the resistance towards sliding. Concerning the shear reinforcement the question is to which extent the bent up bars from the transverse reinforcement in the middle part should be incorporated. These bars are bent up and should therefore (at least to some extent) be incorporated. It has been chosen to fully take these bent up bars into account. The reinforcement utilized as shear reinforcement in the cross section is shown in figure 5.

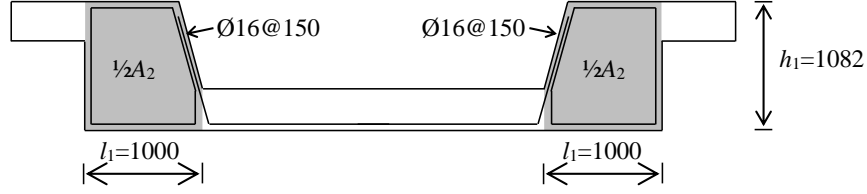


Figure 5. Only reinforcement utilized in carrying the shear force is sketched

On the basis of these assumptions the capacity is again found by using the work equation and minimized with respect to β . The optimization leads to $P = 8.9$ MN and is found for $\beta = 32.4^\circ$

As mentioned, the “classic shear mechanism” shown in figure 4 is not geometrically possible. A punching-mechanism involving two symmetrical failure lines is admissible but will lead to twice the capacity, as the dissipation is simply multiplied with a factor of 2, and thus $P = 17.8$ MN

4.3 Mechanism 3 (Local shear and bending)

In contrast to mechanism 2, a geometrically possible mechanism is shown in Figure 6. The part on the right side of the concentrated load rotates around the rotation point determined in the analysis of the bending mechanism. As the rotation point, with good approximation, is located at the level of the longitudinal reinforcement in the bottom of the beam there will be no contribution from this reinforcement. Due to the rotation the displacement vector is not vertical above this point on the inclined failure line originating from the concentrated load. The vertical component of the displacement vector under the concentrated load is again defined as u . The dissipation from the inclined yield line is determined based on the displacement vector in the centre of the beam, u_1 . This is an approximation as both α_1 and u_1 varies along the yield line. The deviation on the calculated dissipation between this approximation for α_1 and u_1 and applying the correct expression is, however, very small. The contribution from the plastic hinge at the right side of the rotating part is identical to the contribution determined in the analysis of mechanism 1.

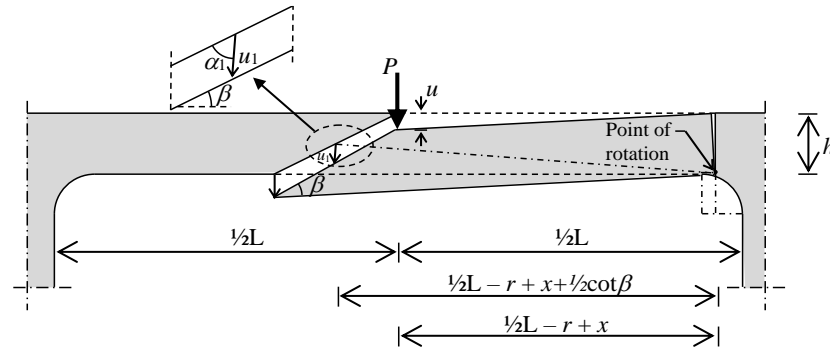


Figure 6. Mechanism 3. Combined shear and bending mechanism. Local mechanism

The optimal solution is found for $\beta = 32.8^\circ$ leading to $P = 13.1$ MN. It is noted, that the additional contribution from the rotation near the support is seen to provide a significant contribution to the capacity.

4.4 Mechanism 4 (Global shear and bending)

By further considering the moment capacity of the beams, it is observed that by moving the plastic hinge to the right span, and requiring an additional plastic hinge in the column, the resulting moment capacity will be considerable smaller than the configuration just considered in mechanism 3.

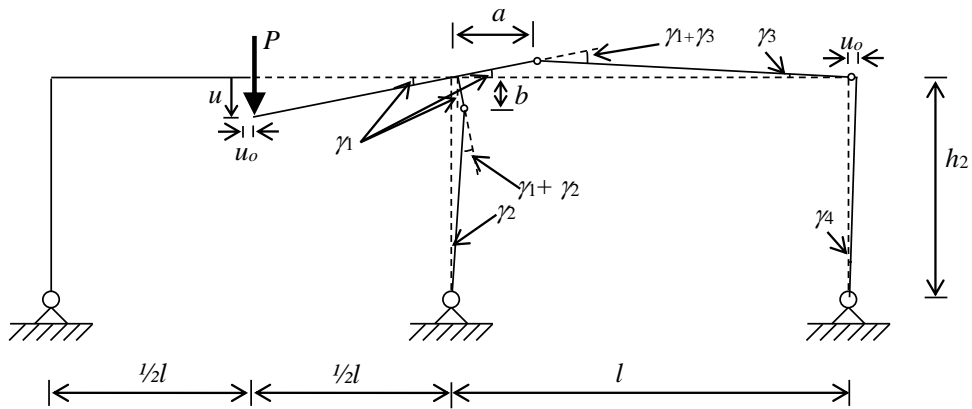


Figure 7. Mechanism 4

The angle of rotation is of the same magnitude, whereby the dissipation will be much smaller, and thus leading to a smaller calculated capacity, and thus more critical mechanism. The mechanism is sketched in Figure 7 and 8. The plastic hinge in the middle column is placed just outside of the circular part between column and beam, that is 700 mm from underneath the bottom of the beams. A horizontal displacement u_o is, as shown in Figure 9, introduced as an additional free kinematic parameter.

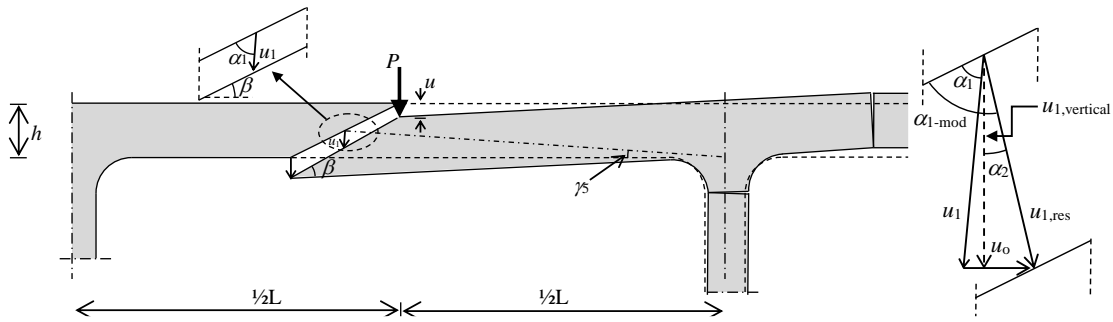


Figure 8. Mechanism 4. Combined shear and bending mechanism

Figure 9.

Optimum is found for $\beta = 35.3^\circ$, $a = 3000$ mm, $u_o = 0.061$ and $\gamma_3 = \gamma_4$ (no hinge at the outer right corner). The mechanism renders the capacity $P = 11.6$ MN. Of the three kinematically admissible mechanisms considered, this is therefore the most critical.

5. Discussion

The on-site test revealed a capacity of 11.7 MN with respect to the concentrated load P , and the capacity corresponding to the most critical mechanism was found to be 11.6 MN which is very close to the measured capacity. The critical mechanism includes a sliding failure near the concentrated loads. Photos clearly support the presence of a shear failure at that position, see Figure 10.



Figure 10. Observed shear failure next to concentrated loads [3]

In addition, the critical mechanism includes plastic hinges in the columns/walls at mid span as well as in the adjacent bridge deck. With respect to the later it has not been possible to find pictures of the adjacent span that could reveal the presence of larger cracks or upward deflections. On the con-

trary, the photos in Figure 11 indicates a plastic hinge in the top of the column. In this connection, it should be emphasized that the model is based on incremental displacements and not absolute displacements. In the present case it is reasonable to conclude that the photos documents the formation of both the sliding failure as well the plastic hinges.

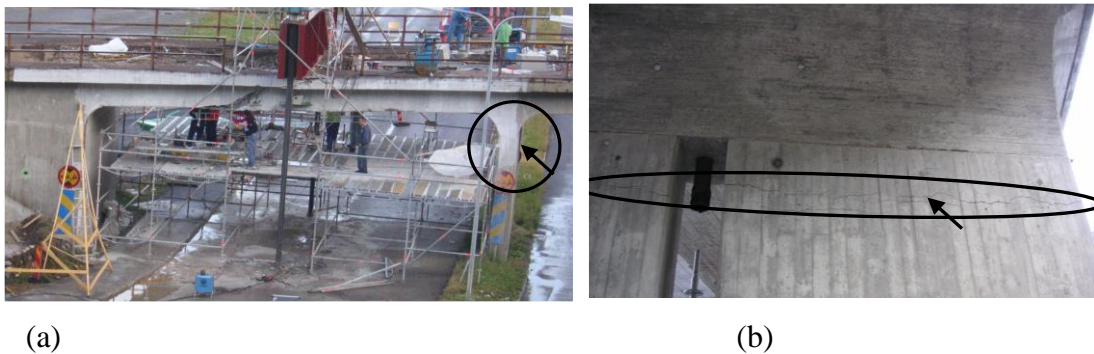


Figure 11. (a) a clear kink is seen at the top of the column (b) clear horizontal cracks at the top of the column.

In [3] a range of different numerical models were analysed, and Figure 12 illustrates the crack pattern at peak load ($P=10.5$ MN) according to a non-linear model developed using ATENA 2D. Severe web cracking near the concentrated load indicates significant influence of shear at that location. In addition, large cracks and plastic deformation are presents in top of columns/wall, and in the adjacent span.



Figure 12. Crack pattern at peak load $P=10.5$ MN. Cracks larger than 0.5 mm. Taken from [3].

6. Conclusion

Simple modelling based on rough material modelling not only provides a good estimate of the capacity on a real scale structures; it also highlights the critical mechanisms and thus the critical parts of the bridge structure. It illustrates, that a clear physical interpretation of the behaviour of the actual structure to be analysed as well as the involved materials it is essential. Beside the good agreement between the calculated and measured capacity the application of the upper bound approach also points out the critical parts of the bridge, as shown in Figure 8. The results are supported by both on-site observations and non-linear modelling.

References

- [1] Bagge, N., Popescu, C, Elfgren, L. (2018). Failure tests on concrete bridges: Have we learnt the lessons? *Structure and Infrastructure Engineering*, Vol. 14, no. 3, 292–319. <https://doi.org/10.1080/15732479.2017.1350985>
- [2] Lantsoght E., Yang, Y., Boer A.D., Hordijk, D.A. (2016). Ruytenschildt Bridge: Field and laboratory testing, *Engineering Structures*, Vol. 128, 111–123. <https://doi.org/10.1016/j.engstruct.2016.09.029>
- [3] Elfgren, L., Enochsson, O., Thun, H. (2008). Field Test of a concrete bridge in örnskoldsvik, Sweden. Deliverable D7.3 (SB-7.3), *Sustainable bridges - Assessment for future traffic demands and longer lives*. Available from www.sustainablebridges.net.

- [4] Henriksen, A., Schmidt, J. W., Engelund, S. (2018). Vejdirektoratet gennemfører bæreevneforsøg på broer (in Danish) *Trafik & Veje*, Maj, 59–61.
- [5] Bagge, N. (2009). Demonstration and examination of a procedure for successively improved structural assessment of concrete bridges. *Structural Concrete*, 1–24.
<https://doi.org/10.1002/suco.201900265>
- [6] Faber, M.H., Val, D.V., Stewart, M.G. (2000) Proof load testing for bridge assessment and upgrading, *Engineering Structures*, Vol. 22, 1677-1689, [https://doi.org/10.1016/S0141-0296\(99\)00111-X](https://doi.org/10.1016/S0141-0296(99)00111-X)
- [7] Lantsoght, E., van der Veen, C, de Boer, A and Hordijk, DA. (2017) Proof load testing of reinforced concrete slab bridges in the Netherlands, *Structural Concrete*, 18: 597– 606.
<https://doi.org/10.1002/suco.201600171>
- [8] von Fintel, L., Michaelsen, L.S. (2019). Assessment of Capacity of a RC Bridge in Örnköldsvik, MSc Thesis, Aarhus School of Engineering, Aarhus University, Denmark
- [9] Nielsen, M. P., Hoang, L.C. (2011). *Limit Analysis and Concrete Plasticity*, 3. edition, CRC Press, Taylor & Francis Group

A form finding problem – the end supported cantilever beam

Bo G Hellers, prof em KTH

Håkan Sundquist, prof em KTH

1. Introduction - the problem

The idea behind this form finding problem was initiated by the late professor Sven Sahlin, our outstanding teacher and colleague. He was a professor in Structural engineering, at Chalmers (CTH) in Gothenburg and later at the Royal Institute of Technology (KTH) in Stockholm.

A one span “Euler-Bernoulli” beam with variable section is studied. The task is to find the variation of bending stiffness $EI(x)$ that gives the largest hogging moment, M_A , at the clamped point A. The stiffness relation between the ends is “ n ” according to Figure 1.1. The stiffness variation between A and B is free. The loading q is constant along the beam. The modulus of elasticity, E , is assumed constant.

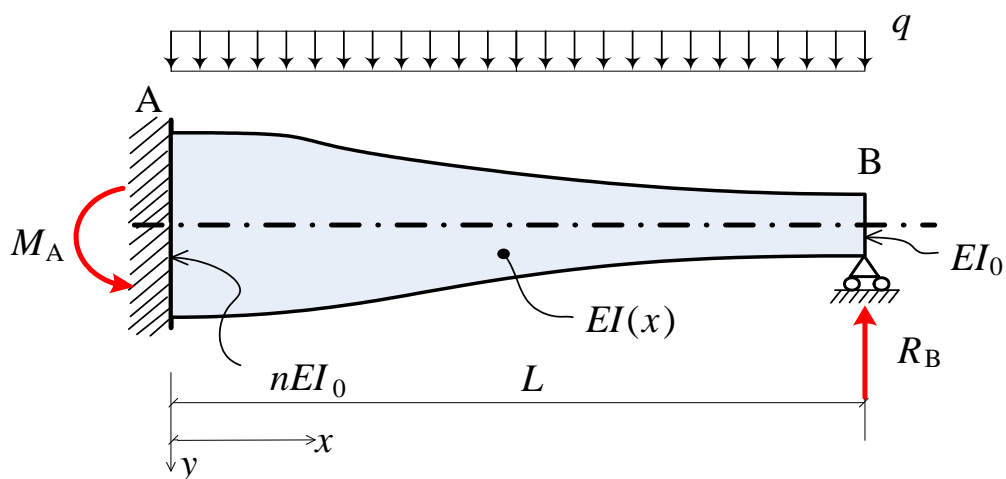


Figure 1.1 Beam with variable bending stiffness. The direction of the hogging moment is considered positive as shown.

1.1 Some general discussion

If the second moment of area is constant along the beam, $n = 1$, the hogging moment is

$$M_{A,\min} = \frac{qL^2}{8} \quad (1-1)$$

restricting this study to $n \geq 1$. Is it possible to find a distribution of $EI(x)$ that leads to $R_B = 0$? If such a case exists the hogging moment would be

$$M_{A,\max} = \frac{qL^2}{2} = \beta \frac{qL^2}{8} (\beta = 4) = 4M_{A,\min} \quad (1-2)$$

Obviously, we are looking for values

$$M_A = \beta \frac{qL^2}{8}; \text{ where } 1 \leq \beta \leq 4 \quad (1-3)$$

1.2 General equations for "Euler-Bernoulli Beams"

The equation describing this theory gives the relationship between the deflection of the beam and the applied load:

$$\frac{d^2}{dx^2} \left(EI(x) \frac{d^2 y}{dx^2} \right) = q \quad (1-4)$$

The curve $y(x)$ describes the deflection y of the beam at some position x (recall that the beam is modelled as a one-dimensional object). q is a distributed load, in other words a force per unit length.

Note that E is the modulus of elasticity and that $I(x) \neq 0$ is the second moment of area (area moment of inertia). $I(x)$ must be calculated with respect to the centroidal axis perpendicular to the applied loading. For an Euler-Bernoulli beam (not under axial loading) this axis is called the neutral axis.

Successive derivatives of y have important meanings

$$y \text{ is the deflection} \quad (1-5)$$

$$\frac{dy}{dx} = \theta \text{ is the slope deflection of the beam at point } x. \quad (1-6)$$

$$M(x) = -EI(x) \frac{d^2 y}{dx^2} \text{ is the bending moment at any point } x \quad (1-7)$$

and

$$Q(x) = \frac{d}{dx} M(x) = -\frac{d}{dx} \left(EI(x) \frac{d^2 y}{dx^2} \right) \text{ is the shear force in the beam at any point } x. \quad (1-8)$$

2. Solutions for continuous variation of beam stiffness

2.1 Introduction

Equation (1-4) is re-written for the case $q = \text{constant}$

$$\frac{d^2}{dx^2} \left(EI(x) \frac{d^2 y}{dx^2} \right) = q \quad ; \quad \frac{d^2}{dx^2} \left(I(x) \frac{d^2 y}{dx^2} \right) = \frac{q}{E} \text{ (const.)} \quad (2-1)$$

This equation can be integrated twice

$$I(x) \frac{d^2 y}{dx^2} = \frac{q}{E} \frac{x^2}{2} + Cx + D \quad (2-2)$$

where C and D are unknown constants. After rewriting

$$-M(x) = \frac{qx^2}{2} + CEx + DE \quad (2-3)$$

$$\text{But } M(L) = 0 \Rightarrow M(x) = (L-x) \left[\frac{q}{2}(L+x) + CE \right]$$

This equation indicates that $M(x)$ is a second order distribution, c.f. Figure 2.4, but the equation does not lead to a solution, since the constant C is still unknown. Going back to equation (1-4) and developing:

$$\frac{d}{dx} \left(\frac{dI(x)}{dx} \frac{d^2 y}{dx^2} + I(x) \frac{d^3 y}{dx^3} \right) = \frac{q}{E} \quad (2-4)$$

$$\frac{d^2 I(x)}{dx^2} \frac{d^2 y}{dx^2} + 2 \frac{dI(x)}{dx} \frac{d^3 y}{dx^3} + I(x) \frac{d^4 y}{dx^4} = \frac{q}{E} \quad (2-5)$$

The task is to find the largest numerical value of $M_{x=0} = \left[-EI(x) \frac{d^2 y}{dx^2} \right]_{x=0}$

It is hard to solve Eq. (2-5) analytically when the moment of inertia varies along the beam, so let's look at a numerical solution.

2.2 Numerical solution of Eq. (2-5)

A central difference scheme is used to find a solution of Euler-Bernoulli beam equation. The numbering of points is shown in Figure 2.1 below

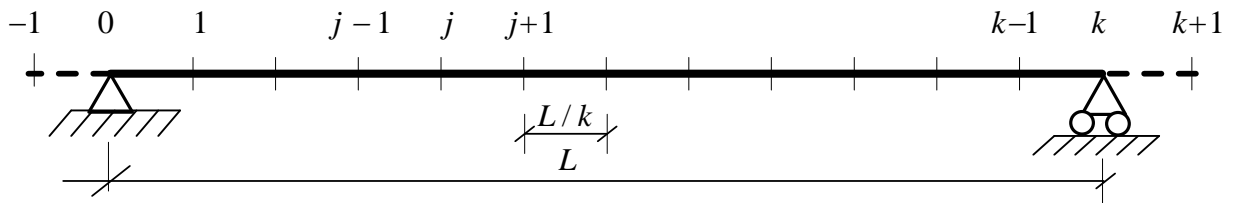


Figure 2.1 To solve the problem using the finite difference method equidistant points along the beam are defined as shown in the figure.

The beam length L is divided in k segments with length $\lambda = L/k$ and the points are numbered according to Figure 2.1. Central differences of the first order are used.

$$\frac{dy}{dx} = \frac{1}{2\lambda} (-y_{j-1} + y_{j+1}) + O(\lambda^2) \quad (2-6)$$

$$\frac{d^2 y}{dx^2} = \frac{1}{\lambda^2} (y_{j-1} - 2y_j + y_{j+1}) + O(\lambda^2) \quad (2-7)$$

$$\frac{d^3 y}{dx^3} = \frac{1}{2\lambda^3} (-y_{j-2} + 2y_{j-1} - 2y_{j+1} + y_{j+2}) + O(\lambda^2) \quad (2-8)$$

$$\frac{d^4 y}{dx^4} = \frac{1}{\lambda^4} (y_{j-2} - 4y_{j-1} + 6y_j - 4y_{j+1} + y_{j+2}) + O(\lambda^2) \quad (2-9)$$

The notation $O(\lambda^2)$ “ordo” is used to describe the remaining terms in the series approximation of the derivatives and show that the remaining terms are here of the order λ^2 . This in turn shows that the accuracy gets better the more segments that are used in the beam to approximate the derivatives.

The following formula Eq. (2-10) is valid for an interior point at the beam where the notation $\lambda = L/k$ is used

$$\begin{aligned} & \frac{1}{\lambda^2} \left(\frac{d^2 I}{dx^2} \right)_j (y_{j-1} - 2y_j + y_{j+1}) + \frac{2}{2\lambda^3} \left(\frac{dI}{dx} \right)_j (-y_{j-2} + 2y_{j-1} - 2y_{j+1} + y_{j+2}) + \\ & + \frac{I_j}{\lambda^4} (y_{j-2} - 4y_{j-1} + 6y_j - 4y_{j+1} + y_{j+2}) = \frac{q}{E} \end{aligned} \quad (2-10)$$

At the end A the following border conditions apply

$$\begin{aligned} y_0 &= 0 \\ y_{-1} &= GST \cdot y_{+1} \end{aligned} \quad (2-11)$$

where $GST = 1$ gives clamped support and $GST = -1$ gives simple support

At end B the following border conditions apply

$$\begin{aligned} y_k &= 0 \\ y_{k+1} &= GSL \cdot y_{k-1} \end{aligned} \quad (2-12)$$

where $GSL = 1$ gives clamped support and $GSL = -1$ gives simple support.

Simple variation of $I(x)$ considering Eqs. (2-11) and (2-12) is tried in the following examples. To solve Eq. (2-5) using Eq. (2-1), we need the first and second derivatives:

$$\begin{array}{l} \text{First} \\ \text{order} \end{array} \quad I(x) = nI_0 - (n-1)I_0 \frac{x}{L} ; \quad \frac{dI(x)}{dx} = -(n-1)I_0 \frac{1}{L} ; \quad \frac{d^2 I(x)}{dx^2} = 0 \quad (2-13)$$

$$\begin{array}{l} \text{Second} \\ \text{order} \end{array} \quad I(x) = nI_0 - (n-1)I_0 \left(\frac{x}{L} \right)^2 ; \quad \frac{dI(x)}{dx} = -2(n-1)I_0 \frac{x}{L^2} ; \quad \frac{d^2 I(x)}{dx^2} = -2(n-1)I_0 \frac{1}{L^2} \quad (2-14)$$

$$\begin{array}{l} \text{Third} \\ \text{order} \end{array} \quad I(x) = nI_0 - I_0(n-1) \left[3 \left(\frac{x}{L} \right)^2 - 2 \left(\frac{x}{L} \right)^3 \right] ; \quad \frac{dI(x)}{dx} = -I_0(n-1) \left(6 \frac{x}{L^2} - 6 \frac{x^2}{L^3} \right) ; \quad (2-15)$$

$$\frac{d^2 I(x)}{dx^2} = -I_0(n-1) \frac{6}{L^2} \left[1 - 2 \frac{x}{L} \right]$$

Note that in the third order case the following relation applies:

$$E \left(\frac{dI(x)}{dx} \right)_{x=0} = E \left(\frac{dI(x)}{dx} \right)_{x=L} = 0 \quad (2-16)$$

Variations for the modulus of elasticity for Eqs. (2.13) – (2.15) is displayed for the case $n = 10$ in Figure 2.2.

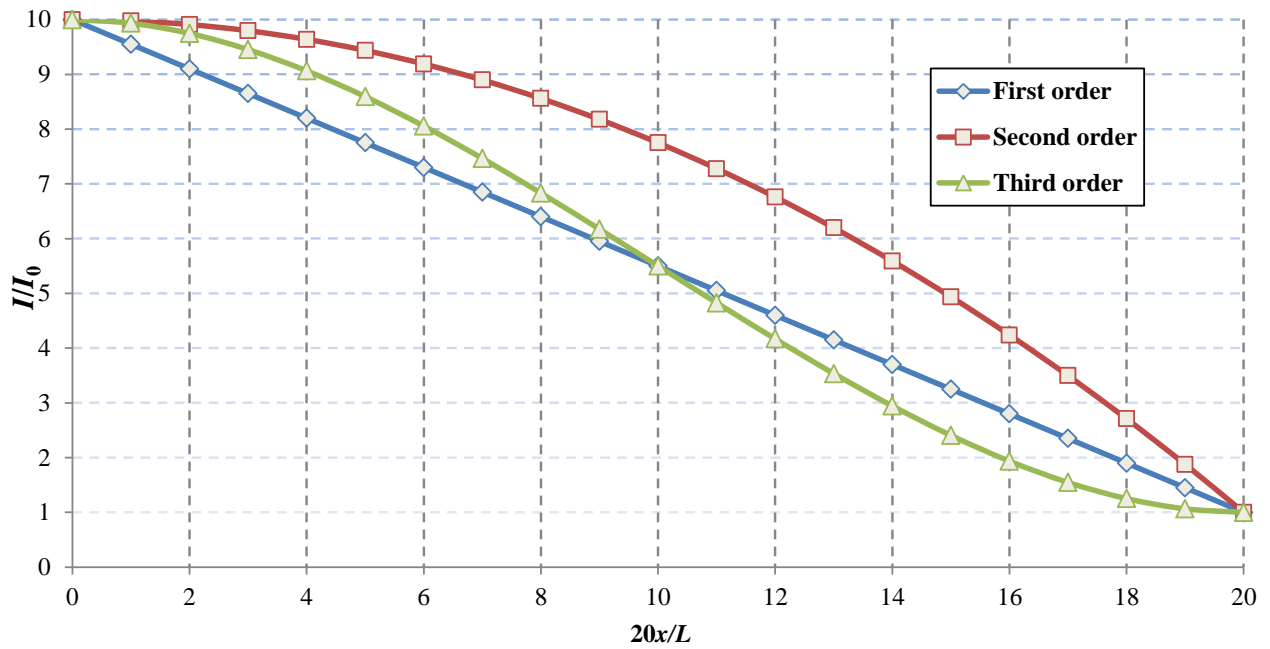


Figure 2.2 Variation of stiffness for the three cases Eqs. (2.13) – (2.15) and end stiffness relation $n = 10$.

	$n = 1$	$n = 10$	$n = 50$	$n = 100$	$n = 200$	$n = 1000$
Eq. (2.13)	0,996	1,247	1,308	1,319	1,324	1,329
Eq. (2.14)	0,996	1,264	1,350	1,366	1,375	1,382
Eq. (2.15)	0,996	1,343	1,517	1,586	1,671	2,064

Table 2.1 Hogging moment $M_A / (qL^2 / 8)$ for a variation of n according to the three different simple variation of $I(x)$. Note that $\lim_{n \rightarrow \infty} \frac{8M_A}{qL^2} = 2$, c.f. section 2.3. Also note the slow convergence for first and second order variation.

The variation according to Eq. (2.15) gives no parameter for variation of the form of the curve. A fourth order curve gives one more parameter to vary.

$$I(x) = nI_0 - I_0(n-1) f\left(\frac{x}{L}, \kappa\right) \tag{2-17}$$

The general form of a fourth order equation is

$$EI(x) = A\left(\frac{x}{L}\right)^4 + B\left(\frac{x}{L}\right)^3 + C\left(\frac{x}{L}\right)^2 + D\left(\frac{x}{L}\right) + E \tag{2-18}$$

Again, using the boundary values:

$$x = 0 \rightarrow EI(x) = nEI_0 ; E \frac{dI(x)}{dx} = 0$$

$$x = L \rightarrow EI(x) = EI_0 ; E \frac{dI(x)}{dx} = 0$$

and a parameter defined at $x/L = 0,5 \rightarrow \kappa \cdot 1$. The result using the notation $h = 2\kappa - 1$ is

$$\frac{EI(x)}{EI_0} = n - (n-1) \cdot \left[8h \left(\frac{x}{L}\right)^4 - 2(1+8h) \left(\frac{x}{L}\right)^3 + (8h+3) \left(\frac{x}{L}\right)^2 \right] \quad (2-19)$$

For some values of κ the diagram below is achieved for $EI(x)$.

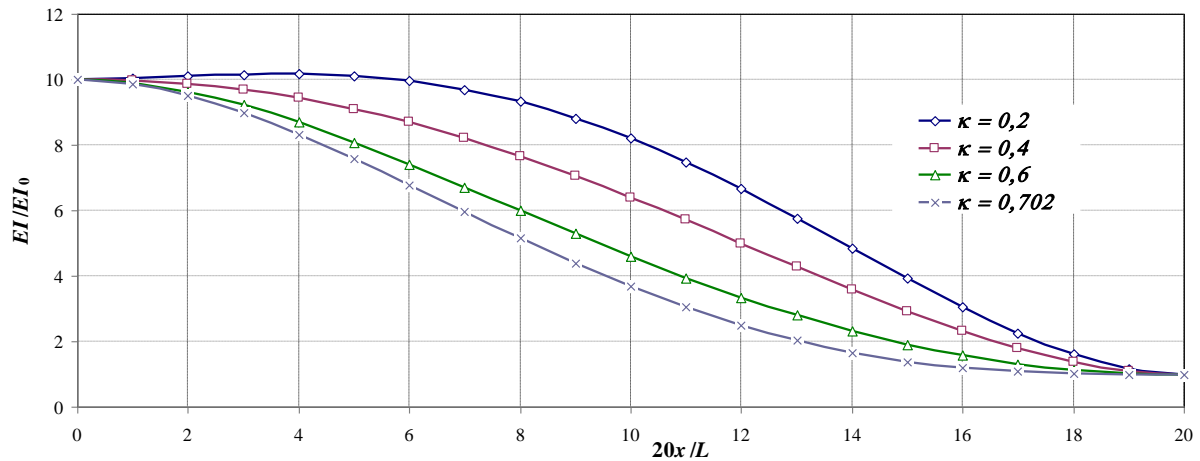


Figure 2.3 An assumed variation of stiffness for a forth order function and end stiffness relation $n = 10$.

The moment distribution is shown in Figure 2.4. Only strictly decreasing values for EI from the clamped support to the simple support are considered here, except in the case $\kappa = 0,2$. It is possible to find higher values for the hogging moment if the stiffness values are much smaller than EI_0 close to support B. At the end a degenerated case with a hinge ($EI = 0$) close to the support is formed giving $\beta \rightarrow 4$.

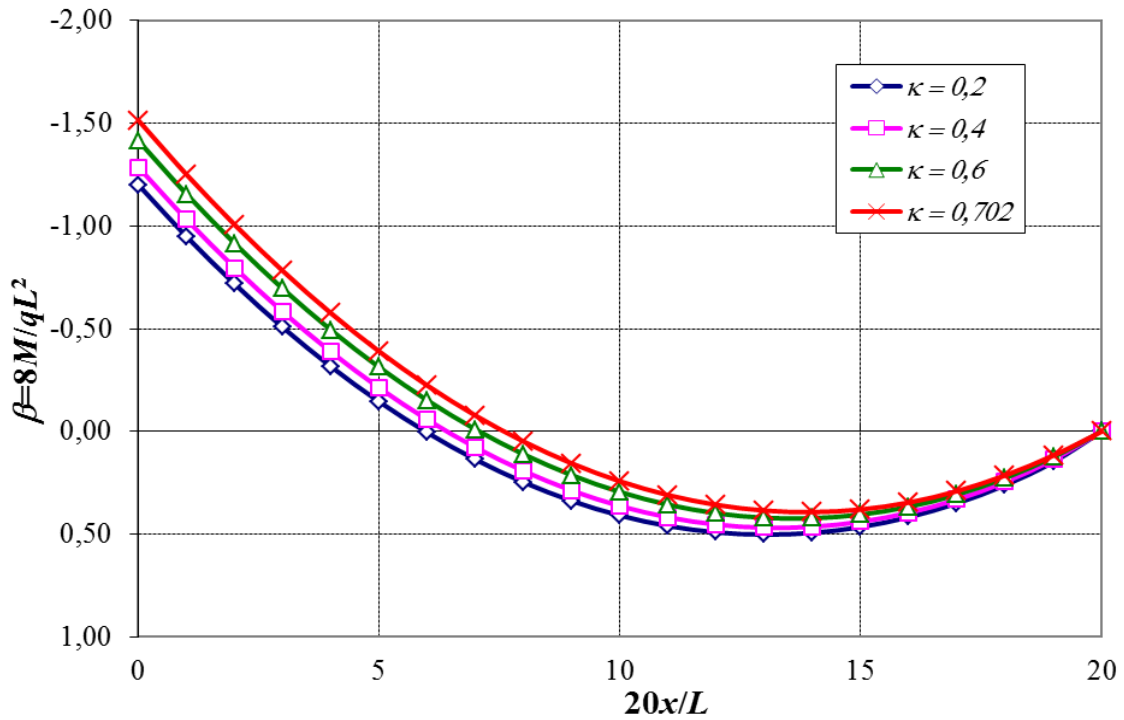


Figure 2.4 Moment distribution for an end stiffness relation $n = 10$ and different values of the parameter κ , all except the case $\kappa = 0,2$ strictly decreasing stiffness from A to B.

With the EI -variation according to Eq. (2-17) the hogging moment at A is shown for different values of κ and $n = 10$ in Table 2.2 below.

κ	0,2	0,3	0,4	0,5	0,6	0,702
$M / (qL^2 / 8)$	1,201	1,240	1,286	1,343	1,416	1,514

Table 2.2 Hogging moment at A for a variation according to a fourth order equation for different values of κ and $n = 10$. The (minimum) optimum is reached at $\kappa = 0,702$.

For different values of n and the optimized value of κ the hogging moment is shown in **Table 2.3**.

n	10	17	20	50	100	200	1000
$M / (qL^2 / 8)$	1,514	1,631	1,666	1,853	1,978	2,077	1,938

Table 2.3 Hogging moment at A for a variation according to a fourth order equation for different values of n and an optimized value of κ . Again, note that $\lim_{n \rightarrow \infty} \frac{8M_A}{qL^2} = 2$. Note the rapid convergence in case of a fourth order variation.

2.3 The case $n \rightarrow \infty$

Any distribution of bending stiffness along a beam can be summarized by:

$$\sum_{k=1}^{k=m} \mu_k = 1 \left\{ \begin{array}{l} nI_0 - (n-1)I_0 \frac{x}{L} \quad \square \quad \mu_1 \\ nI_0 - (n-1)I_0 \left(\frac{x}{L}\right)^2 \quad \square \quad \mu_2 \\ \dots \\ nI_0 - (n-1)I_0 \left(\frac{x}{L}\right)^m \quad \square \quad \mu_m \end{array} \right. \quad (2-18)$$

The previous example used $\mu_2 = 3$, $\mu_3 = -2$

These are all continuous functions of x , which is important in the following:

Taking $m = 1$ leads to the bending equation

$$Ey''I_0 \left(n + \frac{x/L}{1-x/L} \right) = M_A - q \frac{xL}{2} \quad (2-19)$$

Taking $m = 2$ – while $\mu_1 = 0$ – leads to

$$Ey''I_0 \left[n \left(1 + \frac{x}{L} \right) + \frac{(x/L)^2}{1-x/L} \right] = M_A - q \frac{xL}{2} \quad (2-20)$$

Adding to a general form

$$EI_0 n y''(x) \sum_{k=1}^m \mu_k \left[1 - \left(1 - \frac{1}{n} \right) \left(\frac{x}{L} \right)^k \right] \left(1 - \frac{x}{L} \right)^{-1} = M_A - q \frac{xL}{2} \quad (2-21)$$

since

$$\lim_{n \rightarrow \infty} y''(x) \equiv 0 \quad (0 \leq x < L) \quad (2-22)$$

it is possible to conclude that

$$M_A - q \frac{xL}{2} \Big|_{x=L} \rightarrow 0 \quad (2-23)$$

$$M_A = \frac{qL^2}{2} \quad (\beta = 4)$$

in a degenerated case, as previously stated.

In a continuous case $x < L$, the analysis leads to

$$\begin{aligned} EI_0 \lim_{n \rightarrow \infty} n \int_0^L \left\{ y''(z) \left(1 - \frac{z}{L} \right)^{-1} \sum_{k=1}^m \mu_k \left[1 - \left(1 - \frac{1}{n} \right) \left(\frac{z}{L} \right)^k \right] \right\} dz &= 0 = \\ = \int_0^L \left(M_A - q \frac{zL}{2} \right) dz & \end{aligned} \quad (2-24)$$

giving

$$M_A = q \frac{L^2}{4} \quad (\beta = 2)$$

This result is independent of the specific distribution of bending stiffness along the beam.

3. Stepped haunch

A discontinuous stepped haunch may open the area of definition, $2 < \beta \leq 4$, for limited values of “ n ”, see Figure 3.1.

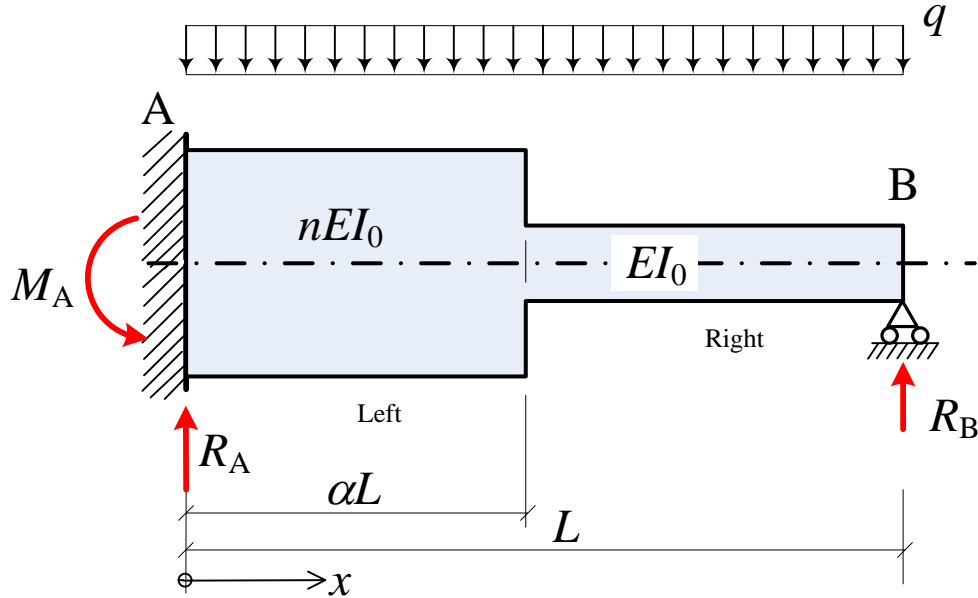


Figure 3.1 Schematic figure showing the studied beam with stepped haunch. The figure shows also the notations used. In the following the basic stiffness will have the notation EI_0 .

In this chapter three methods for studying the stepped situation will be discussed; in Section 3.1 an analytical solution, in Section 3.2 a numerical solution and in Section 3.3 optimizing tools in Matlab combined with methods having been used to find the largest value of the hogging moment at the A support.

3.1 Analytical solution for the stepped beam

The equation describing this theory gives the relationship between the beam's deflection and the applied load:

$$\frac{d^2}{dx^2} \left(EI(x) \frac{d^2 y}{dx^2} \right) = q \quad (3.1-1)$$

$y''(x)$ must have equal value, on both sides of a haunch, positioned at $\alpha L (0 \leq \alpha \leq 1)$:

$y''(\alpha L)_{\text{left}} = y''(\alpha L)_{\text{right}}$, but $-y''(x) = \frac{M(x)}{nEI_0}$ to the left and $-y''(x) = \frac{M(x)}{EI_0}$ to the right. This is

only possible if

$$M(\alpha L) = 0 \quad (3.1-1')$$

Using Eq. (3.1-1) for beam part $0 \leq x \leq \alpha L$ gives

$$y'' = -\frac{M(x)}{nEI} = -\frac{1}{nEI} \left(-M_A + R_A x - q \frac{x^2}{2} \right) \quad (3.1-2)$$

Equilibrium gives since $M_B = 0$:

$$-M_A + R_A L - q \frac{L^2}{2} = 0 \Rightarrow R_A = \frac{1}{L} M_A + q \frac{L}{2} \quad (3.1-3)$$

Insertion of Eq. (3.1-3) gives

$$y'' = -\frac{1}{nEI} \left(-M_A + M_A \frac{x}{L} + q \frac{L}{2} x - q \frac{x^2}{2} \right) \quad (3.1-4)$$

After simplification the result is:

$$y'' = -\frac{1}{nEI} \left[-M_A \left(1 - \frac{x}{L} \right) + q \frac{xL}{2} \left(1 - \frac{x}{L} \right) \right] \quad (3.1-5)$$

or

$$y'' = \frac{1}{nEI} \left(M_A - q \frac{xL}{2} \right) \left(1 - \frac{x}{L} \right), \text{ note that } \lim_{n \rightarrow \infty} y''(x) = 0 \quad (3.1-5')$$

Eq. (3.1-5) integrates once

$$y'(x) = -\frac{1}{nEI} \left(-M_A x + M_A \frac{x^2}{2L} + qL \frac{x^2}{4} - q \frac{x^3}{6} \right) + C \quad (3.1-6)$$

$$y'(0) = 0 \Rightarrow C = 0$$

$$y'(\alpha L) = \frac{1}{nEI} \left[M_A \left(x - \frac{x^2}{2L} \right)_{x=\alpha L} + qx^2 \left(\frac{x}{6} - \frac{L}{4} \right)_{x=\alpha L} \right] \quad (3.1-7)$$

Inserting the x -value gives

$$y'(\alpha L) = \frac{1}{nEI} \left[M_A \alpha L \left(1 - \frac{\alpha}{2} \right) - q \frac{\alpha^2}{4} L^3 \left(1 - \frac{2}{3} \alpha \right) \right] \quad (3.1-8)$$

A second integration gives

$$y(x) = -\frac{1}{nEI} \left[-M_A \frac{x^2}{2} + M_A \frac{x^3}{6L} + qL \frac{x^3}{12} - q \frac{x^4}{24} \right] + D \quad (3.1-9)$$

$$y(0) = 0 \Rightarrow D = 0$$

$$y(\alpha L) = \frac{1}{nEI} \left[M_A \frac{\alpha^2 L^2}{2} \left(1 - \frac{\alpha}{3} \right) - qL \frac{\alpha^3 L^3}{12} \left(1 - \frac{\alpha}{2} \right) \right] \quad (3.1-10)$$

Using Eq. (3.1-5') for beam part $\alpha L \leq x \leq L$ gives

$$y'' = \frac{1}{EI} \left(M_A - q \frac{xL}{2} \right) \left(1 - \frac{x}{L} \right) \quad (3.1-11)$$

Eq. (3.1-11) integrates once

$$y'(x) = -\frac{1}{EI} \left(-M_A x + M_A \frac{x^2}{2L} + qL \frac{x^2}{4} - q \frac{x^3}{6} \right) + E_0 \quad (3.1-12)$$

$$y'(\alpha L) = \frac{1}{EI} \left[M_A \left(x - \frac{x^2}{2L} \right)_{x=\alpha L} + qx^2 \left(\frac{x}{6} - \frac{L}{4} \right)_{x=\alpha L} \right] + E_0 \quad (3.1-13)$$

Inserting the x -value gives

$$y'(\alpha L) = \frac{1}{EI} \left[M_A \alpha L \left(1 - \frac{\alpha}{2} \right) - q \frac{\alpha^2}{4} L^3 \left(1 - \frac{2}{3} \alpha \right) \right] + E_0 \quad (3.1-14)$$

A second integration of Eq.(3.1-12) gives

$$y(x) = -\frac{1}{EI} \left[-M_A \frac{x^2}{2} + M_A \frac{x^3}{6L} + qL \frac{x^3}{12} - q \frac{x^4}{24} \right] + E_0 x + F \quad (3.1-15)$$

Inserting the x -value L gives

$$\begin{aligned} y(L) = 0 &= -\frac{1}{EI} \left[-M_A \frac{L^2}{2} + M_A \frac{L^2}{6} + q \frac{L^4}{12} - q \frac{L^4}{24} \right] + E_0 L + F = \\ &= \frac{1}{EI} \frac{L^2}{3} \left(M_A - \frac{qL^2}{8} \right) + E_0 L + F \end{aligned} \quad (3.1-15')$$

$$F = -\frac{1}{EI} \frac{L^2}{3} \left(M_A - \frac{qL^2}{8} \right) - E_0 L \quad (3.1-15'')$$

Inserting the αL – value in Eq. (3.1-15) gives

$$y(\alpha L) = \frac{1}{EI} \left[\frac{M_A}{2} \alpha^2 L^2 \left(1 - \frac{\alpha}{3} \right) - qL \frac{\alpha^3 L^3}{12} \left(1 - \frac{\alpha}{2} \right) \right] + E_0 \alpha L + F \quad (3.1-16)$$

At the connection between the two stiffness parts nEI (Left) and EI (Right), y' and y should have identical values. This leads to the following terms and equations

$$y'(\alpha L)_L = y'(\alpha L)_R :$$

$$\begin{aligned} \frac{1}{nEI} \left[M_A \alpha L \left(1 - \frac{\alpha}{2} \right) - q \frac{\alpha^2}{4} L^3 \left(1 - \frac{2}{3} \alpha \right) \right] &= \\ = \frac{1}{EI} \left[M_A \alpha L \left(1 - \frac{\alpha}{2} \right) - q \frac{\alpha^2}{4} L^3 \left(1 - \frac{2}{3} \alpha \right) \right] + E_0 \end{aligned} \quad (3.1-17)$$

or simplified

$$\frac{1}{EI} \left(1 - \frac{1}{n} \right) \left[M_A \alpha L \left(1 - \frac{\alpha}{2} \right) - q \frac{\alpha^2}{4} L^3 \left(1 - \frac{2}{3} \alpha \right) \right] + E_0 = 0 \quad (3.1-17')$$

$$y(\alpha L)_L = y(\alpha L)_R \text{ gives}$$

$$\begin{aligned} & \frac{1}{nEI} \left[M_A \frac{\alpha^2 L^2}{2} \left(1 - \frac{\alpha}{3}\right) - qL \frac{\alpha^3 L^3}{12} \left(1 - \frac{\alpha}{2}\right) \right] = \\ & = \frac{1}{EI} \left[M_A \frac{\alpha^2 L^2}{2} \left(1 - \frac{\alpha}{3}\right) - qL \frac{\alpha^3 L^3}{12} \left(1 - \frac{\alpha}{2}\right) \right] + E_0 \alpha L + F \end{aligned} \quad (3.1-18)$$

or simplified

$$\frac{1}{EI} \left(1 - \frac{1}{n}\right) \left[M_A \frac{\alpha^2 L^2}{2} \left(1 - \frac{\alpha}{3}\right) - qL \frac{\alpha^3 L^3}{12} \left(1 - \frac{\alpha}{2}\right) \right] + E_0 \alpha L + F = 0 \quad (3.1-18')$$

and

$$E_0 \alpha L + F = -E_0 L(1 - \alpha) - \frac{1}{EI} \frac{L^2}{3} \left(M_A - \frac{qL^2}{8} \right) \quad (3.1-19)$$

Combining Eqs. (3.1-18') and (3.1-19) gives

$$\begin{aligned} & \frac{1}{EI} \left(1 - \frac{1}{n}\right) \left[M_A \frac{\alpha^2 L^2}{2} \left(1 - \frac{\alpha}{3}\right) - qL \frac{\alpha^3 L^3}{12} \left(1 - \frac{\alpha}{2}\right) \right] - \\ & - E_0 L(1 - \alpha) - \frac{1}{EI} \frac{L^2}{3} \left(M_A - q \frac{L^2}{8} \right) = 0 \end{aligned} \quad (3.1-20)$$

Inserting Eq. (3.1-17') in Eq. (3.1-20) gives

$$\begin{aligned} & \frac{1}{EI} \left(1 - \frac{1}{n}\right) \left[M_A \frac{\alpha^2 L^2}{2} \left(1 - \frac{\alpha}{3}\right) - qL \frac{\alpha^3 L^3}{12} \left(1 - \frac{\alpha}{2}\right) \right] \\ & + L(1 - \alpha) \frac{1}{EI} \left(1 - \frac{1}{n}\right) \left[M_A \alpha L \left(1 - \frac{\alpha}{2}\right) - q \frac{\alpha^2}{4} L^3 \left(1 - \frac{2}{3} \alpha\right) \right] \\ & - \frac{1}{EI} \frac{L^2}{3} \left(M_A - q \frac{L^2}{8} \right) = 0 \end{aligned} \quad (3.1-21)$$

Eq. (3.1-21) can by separating M_A from q and L lead to the conclusive formula:

$$M_A = \frac{\left(1 - \frac{1}{n}\right) \alpha^2 (3\alpha^2 - 8\alpha + 6) - 1}{\left(1 - \frac{1}{n}\right) \alpha (\alpha^2 - 3\alpha + 3) - 1} q \frac{L^2}{8} \quad (3.1-22)$$

or

$$\frac{M_A 8}{qL^2} = \beta = \frac{\left(1 - \frac{1}{n}\right) \alpha^2 (3\alpha^2 - 8\alpha + 6) - 1}{\left(1 - \frac{1}{n}\right) \alpha (\alpha^2 - 3\alpha + 3) - 1} = \frac{\text{Numerator}}{\text{Denominator}} \quad (3.1-22')$$

Based on Eq. (3.1-22) β is shown in Table 3.1 and Figure 3.2 as a function of n and α . The more exact values for β must be calculated by derivation of Eq. (3.1-22) according to Eq. (3.1-23)

$$\frac{d}{d\alpha} \left(\frac{M_A 8}{qL^2} \right) = 0 \Rightarrow D \cdot \frac{dN}{d\alpha} - N \cdot \frac{dD}{d\alpha} = 0 \quad (3.1-23)$$

$$\left[\left(1 - \frac{1}{n} \right) \alpha (\alpha^2 - 3\alpha + 3) - 1 \right] \cdot \left[\left(1 - \frac{1}{n} \right) (12\alpha^3 - 24\alpha^2 + 12\alpha) \right] - \left[\left(1 - \frac{1}{n} \right) \alpha^2 (3\alpha^2 - 8\alpha + 6) - 1 \right] \cdot \left[\left(1 - \frac{1}{n} \right) (3\alpha^2 - 6\alpha + 3) \right] = 0 \quad (3.1-24)$$

After simplification the result is

$$\left(1 - \frac{1}{n} \right) \alpha^2 (\alpha^2 - 4\alpha + 6) - 4\alpha + 1 = 0 \quad (3.1-25)$$

By studying Eq. (3.1-25) it is possible that the value $\alpha = 0,5$ can give an interesting value for n . Inserting this α - value in this equation gives the value $n = 17$. Inserting $\alpha = 0,5$ and $n = 17$ in Eq. (3.1-22) gives $\beta_{\max} = 2$. The insertion of Eq. (3.1-25) into Eq. (3.1-22) leads to the general formula:

$$\beta_{\max} = 4\alpha, \text{ with } \alpha \text{ satisfying Eq. (3.1-25)} \quad (3.1-26)$$

What happens with β in the case $n \rightarrow \infty$? Setting this condition in Eq. (3.1-22'), gives the formula

$$\lim_{n \rightarrow \infty} \beta = \frac{\alpha^2 (3\alpha^2 - 8\alpha + 6) - 1}{\alpha (\alpha^2 - 3\alpha + 3) - 1} \quad (3.1-27)$$

Results are given in Table 3.1 and Figure 3.2b.

Alfa\<i>n</i>	10	17	100	1 000	10 000	100 000	1 000 000	∞
0,000	1,00	1,00	1,00	1,00	1,00	1,00	1,00	1,00
0,050	1,13	1,14	1,15	1,15	1,15	1,15	1,15	1,15
0,100	1,26	1,28	1,30	1,30	1,30	1,30	1,30	1,30
0,150	1,38	1,41	1,44	1,45	1,45	1,45	1,45	1,45
0,200	1,49	1,53	1,59	1,60	1,60	1,60	1,60	1,60
0,250	1,59	1,65	1,73	1,75	1,75	1,75	1,75	1,75
0,300	1,68	1,76	1,87	1,90	1,90	1,90	1,90	1,90
0,350	1,75	1,86	2,01	2,05	2,05	2,05	2,05	2,05
0,400	1,79	1,93	2,15	2,19	2,20	2,20	2,20	2,20
0,450	1,81	1,98	2,27	2,34	2,35	2,35	2,35	2,35
0,500	1,79	2,00	2,39	2,49	2,50	2,50	2,50	2,50
0,550	1,74	1,98	2,49	2,63	2,65	2,65	2,65	2,65
0,600	1,66	1,91	2,55	2,77	2,80	2,80	2,80	2,80
0,650	1,54	1,79	2,58	2,91	2,95	2,95	2,95	2,95
0,700	1,41	1,63	2,53	3,02	3,09	3,10	3,10	3,10
0,750	1,28	1,45	2,37	3,11	3,24	3,25	3,25	3,25
0,800	1,16	1,27	2,06	3,13	3,37	3,40	3,40	3,40
0,850	1,08	1,13	1,64	2,97	3,48	3,54	3,55	3,55
0,900	1,02	1,04	1,24	2,35	3,45	3,67	3,70	3,70
0,950	1,00	1,01	1,03	1,32	2,58	3,64	3,83	3,85
0,960	1,00	1,00	1,02	1,17	2,12	3,49	3,84	3,88
0,970	1,00	1,00	1,01	1,08	1,62	3,12	3,81	3,91
0,980	1,00	1,00	1,00	1,02	1,22	2,31	3,61	3,94
0,990	1,00	1,00	1,00	1,00	1,03	1,27	2,48	3,97
1,000	1,00	1,00	1,00	1,00	1,00	1,00	1,00	4 → 1

Table 3.1 β -values as function of n and α , including the case $n = \infty$. Points coloured yellow are “close” to the maximum value. Note that $M(\alpha L) = 0$.

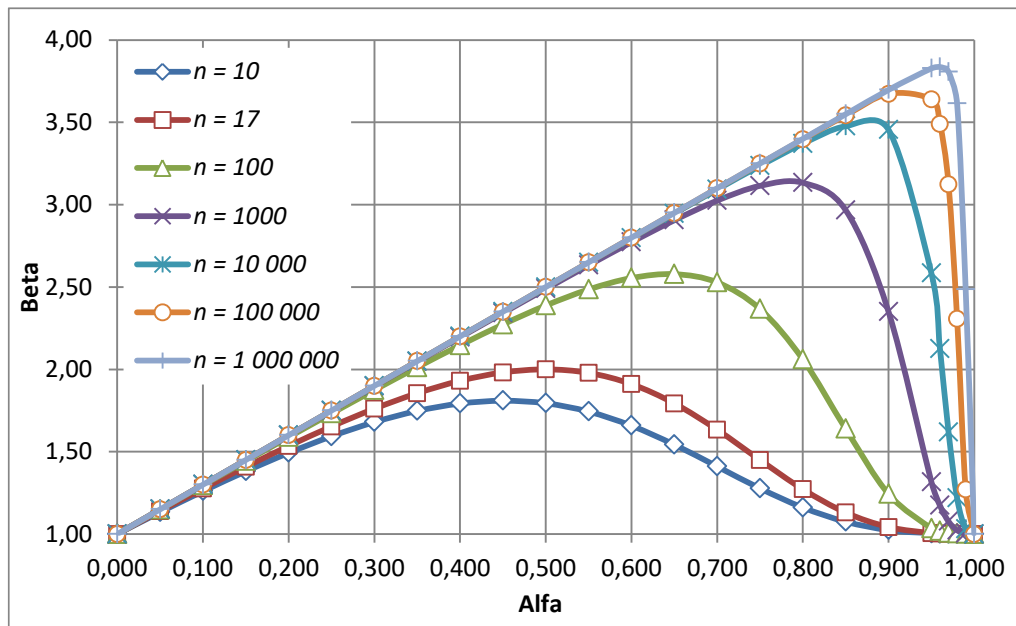


Figure 3.2a β -values as function of n and α . See also Figure 3.2b.

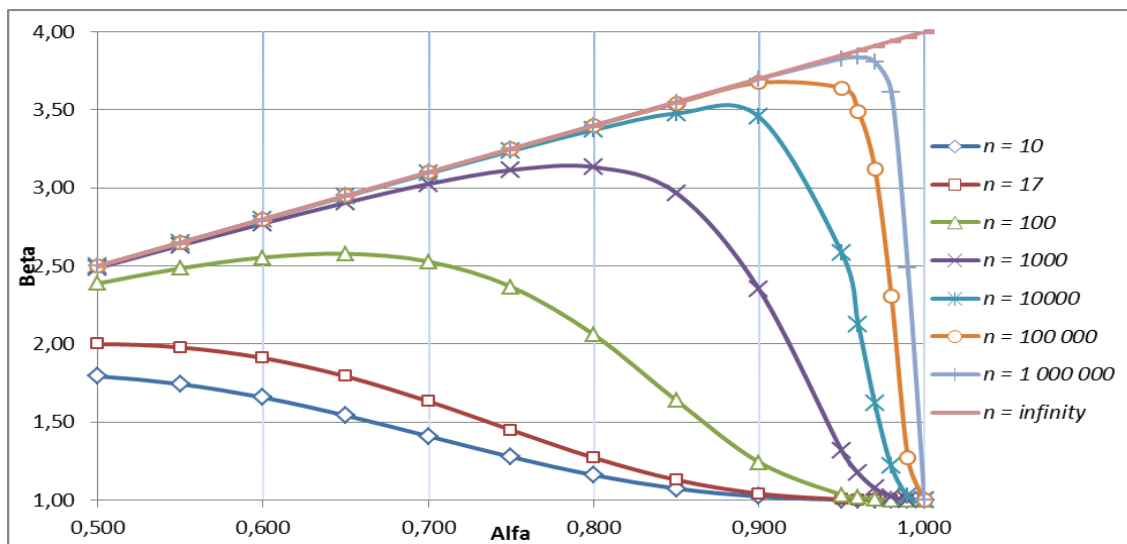


Figure 3.2b β -values as function of n and α . The figure is showing a part of Figure 3.2a and including the case $n \rightarrow \infty$.

The left hand side of Eq. (3.1-25) is shown in Table 3.3 and Figure 3.3.

<i>Alfa</i> \ <i>n</i>	10	17	100	10 000	1 000 000	∞
0,000	1,000	1,000	1,000	1,000	1,000	1,000
0,050	0,813	0,814	0,814	0,815	0,815	0,815
0,100	0,650	0,653	0,656	0,656	0,656	0,656
0,150	0,510	0,515	0,521	0,522	0,522	0,522
0,200	0,389	0,397	0,408	0,410	0,410	0,410
0,250	0,285	0,298	0,313	0,316	0,316	0,316
0,300	0,196	0,214	0,236	0,240	0,240	0,240
0,350	0,121	0,144	0,173	0,178	0,179	0,179
0,400	0,057	0,087	0,122	0,130	0,130	0,130
0,450	0,002	0,039	0,083	0,091	0,092	0,092
0,500	-0,044	0,000	0,052	0,062	0,062	0,063
0,550	-0,083	-0,032	0,029	0,041	0,041	0,041
0,600	-0,117	-0,058	0,011	0,025	0,026	0,026
0,650	-0,146	-0,080	-0,001	0,015	0,015	0,015
0,700	-0,173	-0,098	-0,010	0,008	0,008	0,008
0,750	-0,196	-0,114	-0,016	0,004	0,004	0,004
0,800	-0,219	-0,128	-0,020	0,001	0,002	0,002
0,850	-0,240	-0,141	-0,023	0,000	0,001	0,001
0,900	-0,260	-0,153	-0,026	0,000	0,000	0,000
0,950	-0,280	-0,165	-0,028	0,000	0,000	0,000
1,000	-0,300	-0,176	-0,030	0,000	0,000	0,000

Table 3.3 Value of left hand of Eq. (3.1-25) as a function of *n* and *α*, now completed with the case *n* = 17 and *n* → ∞.

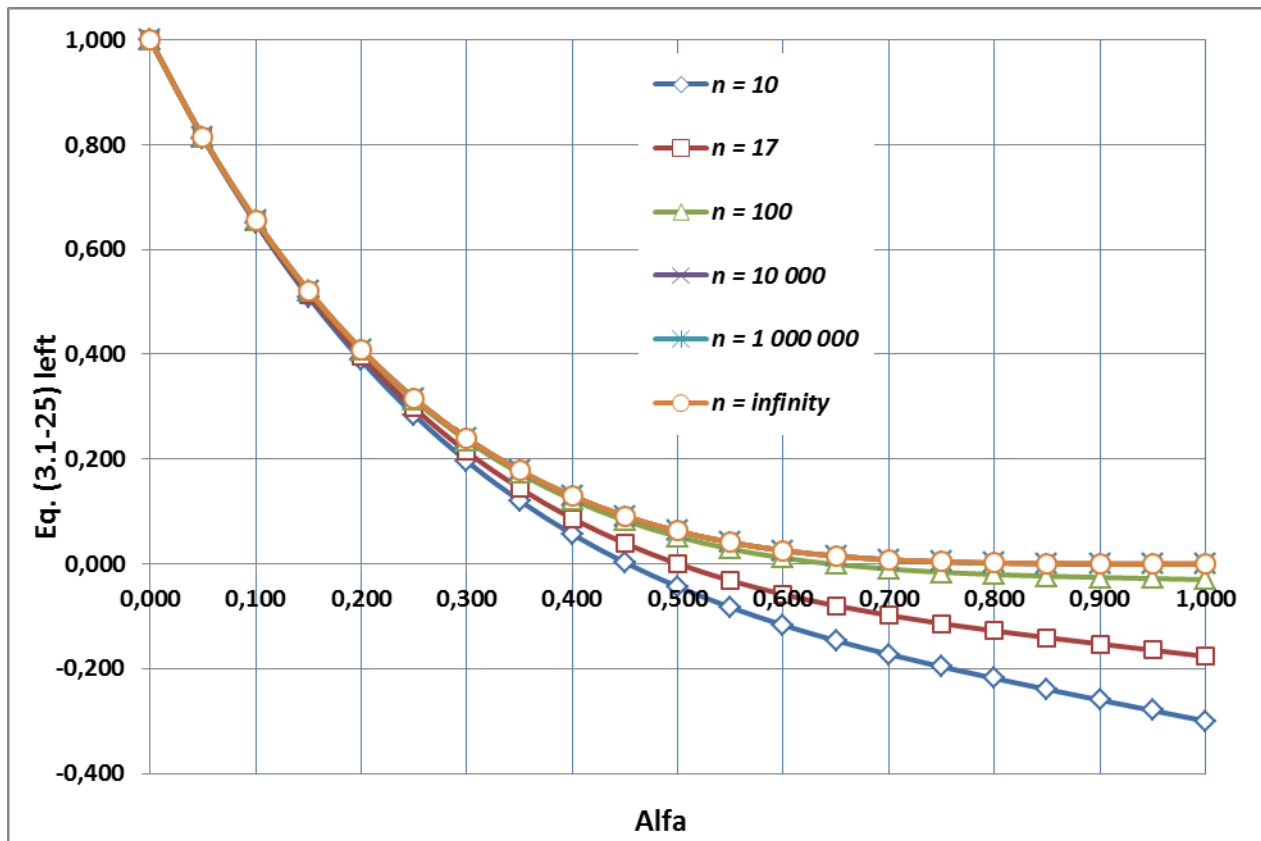


Figure 3.3 Value of left hand of Eq. (3.1-25) as a function of n and α , now completed with the cases $n = 17$ and $n \rightarrow \infty$.

3.2 Numerical solution

A numerical solution can be achieved using the same methodology as was described above in Section 2.2. The abrupt variation of stiffness is at a point $x = \alpha L$, see **Figure 3.4**.

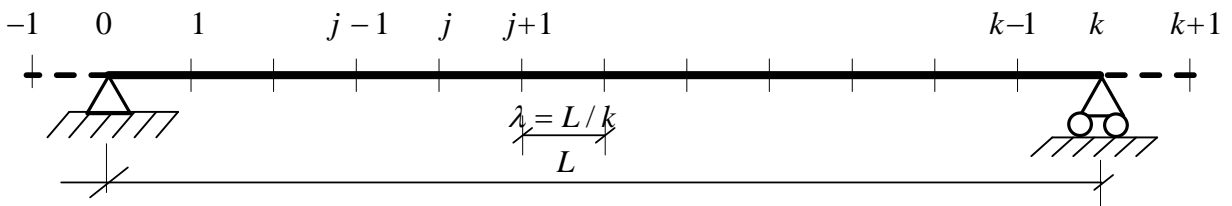


Figure 3.4 To solve the problem using the finite difference method equidistant points along the beam is defined as shown in the figure. At one point m , $x = \alpha L$, the stiffness is reduced from nI_0 to I_0 according to Figure 3.1 and 3.5.

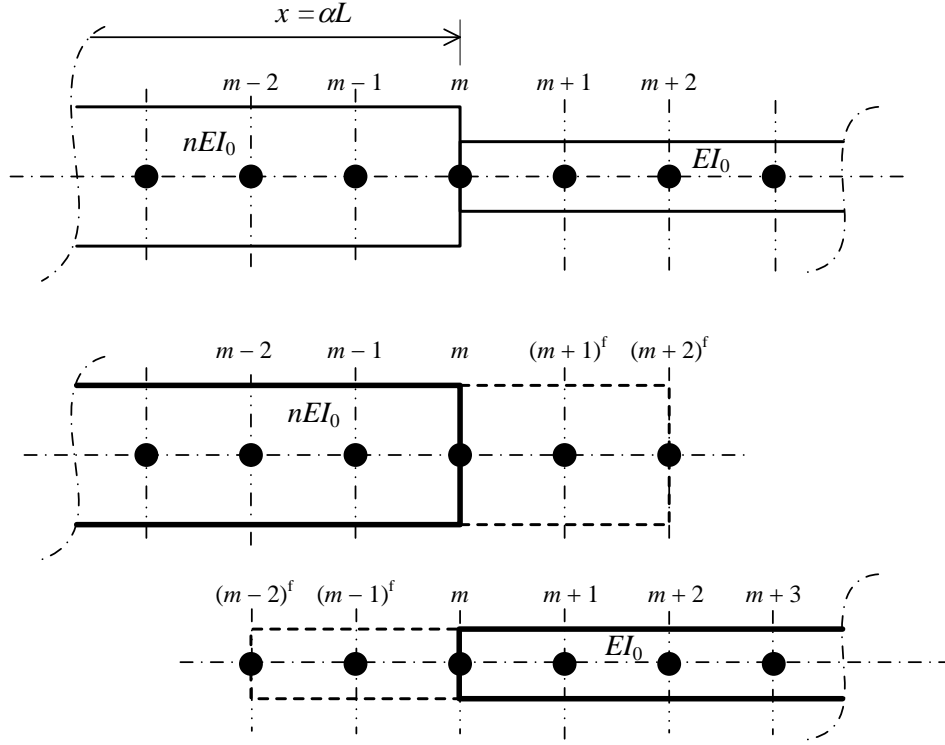


Figure 3.5 The beam part from 0 to point m has stiffness nI_0 and from m to k the stiffness is I_0 .

In this case we must take the abrupt stiffness variation into account according to Eqs. (3.2-1) to (3.2-5). The following relations applies at the point of stiffness variation

$$y_m = y_m^f \quad (3.2-1)$$

$$\frac{1}{2\lambda}(-y_{m-1} + y_{m+1}^f) = \frac{1}{2\lambda}(-y_{m-1}^f + y_{m+1}) \quad (3.2-2)$$

$$\frac{nEI_0}{\lambda^2}(y_{m-1} - 2y_m + y_{m+1}^f) = \frac{EI_0}{\lambda^2}(y_{m-1}^f - 2y_m + y_{m+1}) \quad (3.2-3)$$

$$\frac{nEI_0}{2\lambda^3}(-y_{m-2} + 2y_{m-1} - 2y_{m+1}^f + y_{m+2}^f) = \frac{EI_0}{2\lambda^3}(-y_{m-2}^f + 2y_{m-1}^f - 2y_{m+1} + y_{m+2}) \quad (3.2-4)$$

$$\frac{nEI_0}{\lambda^4}(y_{m-2} - 4y_{m-1} + 6y_m - 4y_{m+1}^f + y_{m+2}^f) = \frac{EI_0}{\lambda^4}(y_{m-2}^f - 4y_{m-1}^f + 6y_m - 4y_{m+1} + y_{m+2}) \quad (3.2-5)$$

Since the segments are the same over the whole beam the above equations can be simplified

$$y_m = y_m^f \quad (3.2-1')$$

$$-y_{m-1} + y_{m+1}^f = -y_{m-1}^f + y_{m+1} \quad (3.2-2')$$

$$ny_{m-1} - 2ny_m + ny_{m+1}^f = y_{m-1}^f - 2y_m + y_{m+1} \quad (3.2-3')$$

$$-ny_{m-2} + 2ny_{m-1} - 2ny_{m+1}^f + ny_{m+2}^f = -y_{m-2}^f + 2y_{m-1}^f - 2y_{m+1} + y_{m+2} \quad (3.2-4')$$

$$ny_{m-2} - 4ny_{m-1} + 6ny_m - 4ny_{m+1}^f + ny_{m+2}^f = y_{m-2}^f - 4y_{m-1}^f + 6y_m - 4y_{m+1} + y_{m+2} \quad (3.2-5')$$

Combining Eqs. (3.2-2) and (3.2-3) give the following relations

$\alpha \setminus n$	10	17	20	50	100	200	1000
0,40	1,788	1,9255	1,9596	2,091	2,140	2,167	2,188
0,45	1,805	1,9762	2,020	2,196	2,266	2,304	2,335
0,50	1,790	1,9950	2,050	2,283	2,381	2,435	2,481

Table 3.4 Optimum hogging moment in a stepped beam for different values of α and n .

Using the numerical method presented in Section 3.2 will lead to approximate solutions, but for the tests shown in Table 3.4, the results are very close to the exact solutions, compare Table 3.2. It is though possible to improve accuracy by dividing the beam into more segments, but it is more efficient to use the “Richardson extrapolation method”.

3.3 Using computer tools to find the largest hogging moment

A PhD student Ignacio Gonzalez at the div. of Structural engineering and bridges at KTH has used optimizing tools in Matlab and analytical methods to find the largest value for the hogging moment at the support. He is confident that the optimized distribution of the moment of inertia leads to the stepped case.

He received the following formulas for finding the position of the step, where for a given n the value of α satisfies Eq. (3.3-1)

$$n + 6n\alpha^2 - 4n\alpha^3 + n\alpha^4 - 6\alpha^2 + 4\alpha^3 - \alpha^4 - 4n\alpha = 0 \quad (3.3-1)$$

and then using this value for calculation of the hogging moment using the following Eq. (3.3-2)

$$\frac{M_A}{qL^2} = n \frac{n - 6n\alpha^2 + 8n\alpha^3 - 3n\alpha^4 + 6\alpha^2 - 8\alpha^3 + 3\alpha^4}{3n^2\alpha^2 - n^2\alpha^3 - 3n^2\alpha + n^2 + n\alpha^3 - 3n\alpha^2 + 3n\alpha} \quad (3.3-2)$$

Eqs. (3.3-1) and (3.3-2) are in principle the same as Eq. (3.1-25) and Eq. (3.1-22), but the author of this section used an approximate method, since Matlab was complicated to use for getting good results for many α -values. Examples of results are shown in Table 3.5.

$n =$	10	20	50	100	200
$\alpha =$	0,452	0,514	0,591	0,645	0,693
$M/(qL^2/8)$	1,809	2,057	2,366	2,579	2,771

Table 3.4 Optimum hogging moment in a stepped beam for different values of α . Note the high precision in relation to the general formula $\beta_{\max} = 4\alpha$.

The result in Table 3.4 and Table 3.3 is in good agreement and it is thus indicated that the stepped variation is the optimal solution of the problem.

3.4 Obviously

The relation between α and β is linear. At the maximum hogging moment

$$\beta_{\max} = 4\alpha, \text{ compare Eq. (3.1-26)}$$

In consequence

$$\alpha = 0,5 \Rightarrow \beta_{\max} = 2,$$

and

$\beta_{\max} > 2$ ($n \geq 17$), since $d\beta/dn > 0$, which is a practical piece of advice to the designer.

By differencing Eq. (3.1-22') we get $d\beta/dn$. We start by analysing the equation

$$\frac{d\beta}{dn} = \frac{d\left(\frac{8M_A}{qL^2}\right)}{dn} = \frac{N \frac{1}{n^2} \alpha^2 (3\alpha^2 - 3\alpha + 3) - T \alpha \frac{1}{n^2} \alpha (\alpha^2 - 3\alpha + 3)}{N^2} \quad (3.1-28)$$

End then analysing the Numinator

$$\begin{aligned} & \left[\left(1 - \frac{1}{n}\right) \alpha (\alpha^2 - 3\alpha + 3) - 1 \right] \cdot \alpha (3\alpha^2 - 8\alpha + 6) - \\ & - \left[\left(1 - \frac{1}{n}\right) \alpha^2 (3\alpha^2 - 8\alpha + 6) - 1 \right] \cdot (\alpha^2 - 3\alpha + 3) = \\ & = \left(1 - \frac{1}{n}\right) \alpha^2 (\alpha^2 - 3\alpha + 3) \cdot (3\alpha^2 - 8\alpha + 6) - \alpha (3\alpha^2 - 8\alpha + 6) - \\ & - \left(1 - \frac{1}{n}\right) \alpha^2 (3\alpha^2 - 8\alpha + 6) \cdot (\alpha^2 - 3\alpha + 3) + (\alpha^2 - 3\alpha + 3) = \\ & = -3\alpha^3 + 8\alpha^2 - 6\alpha + \alpha^2 - 3\alpha + 3 = -3(\alpha^3 - 3\alpha^2 + 3\alpha - 1) = \\ & = -3(\alpha - 1)^3 = 3(1 - \alpha)^3 \end{aligned}$$

Adding the Denominator of Eq. (3.1-22') squared gives (3.1-29)

$$\frac{d(8M_A/qL^2)}{dn} = 3 \frac{(1 - \alpha)^3}{\left[\left(1 - \frac{1}{n}\right) \alpha (\alpha^2 - 3\alpha + 3) - 1 \right]^2} > 0 \quad (3.1-30)$$

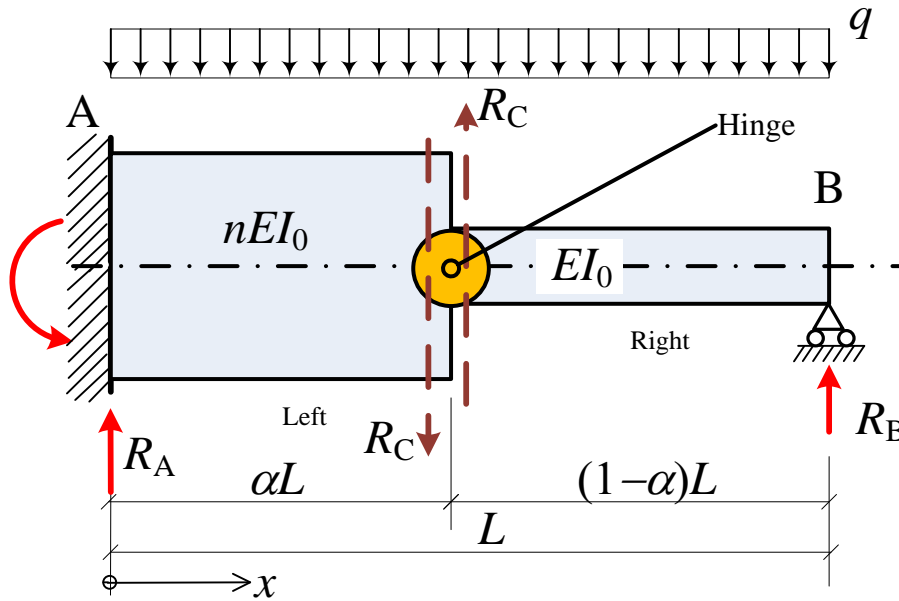
$$\lim_{n \rightarrow \infty} \frac{d(8M_A/qL^2)}{dn} = 3 \frac{(1 - \alpha)^3}{\left[(\alpha - 1)^3 \right]^2} = 3 \frac{1}{(1 - \alpha)^3} > 0$$

3.5 Equilibrium

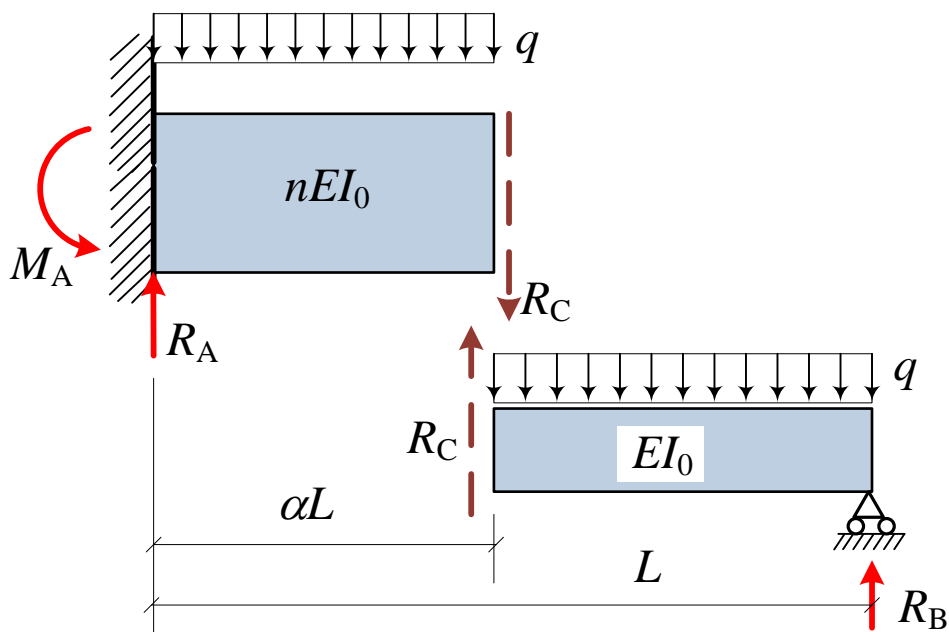
This is a very simple model to illustrate what happens if the moment at the beam haunch generally is equal to zero i.e. $M(\alpha L) = 0$. A continuous variation of $M(x)$ over the hinge, i.e.

$$\frac{M(\alpha L)_L}{nEI_0} = \frac{M(\alpha L)_R}{EI_0} \quad (3.5-1)$$

is only possible when $M(\alpha L) = 0$. A hinge is illustrated at the connection αL between the two beam parts.



Each beam part must be in equilibrium but only two equations are used to eliminate the shear force R_C at the connection.



A moment equation at A gives

$$M_A = \alpha L q \cdot \frac{\alpha L}{2} + R_C \alpha L \quad (3.5-2)$$

A moment equation at B gives

$$qL(1-\alpha) \frac{(1-\alpha)L}{2} - R_C(1-\alpha)L = 0 \quad (3.5-3)$$

or simplified

$$R_C = qL \frac{(1-\alpha)}{2} \quad (3.5-3')$$

Combining Eqs. (3.5-2) and (3.5-3) gives

$$M_A = \frac{qL^2 \alpha^2}{2} + qL \frac{(1-\alpha)}{2} \alpha L = \frac{qL^2}{2} \alpha \tag{3.5-4}$$

and

$$\frac{M_A \cdot 8}{qL^2} = \beta = 4\alpha \tag{3.5-5}$$

which indicates that

$$\beta = \beta_{\max} \text{ at } M(\alpha L) = 0 \tag{3.5-6}$$

and α satisfying Eq. (3.1-25)

Point	0	1	2	3	4	5	6	7	8	9	10	11	12	13	14	15	16	17	18	19	20	
0	1	0	0	0	0	0	0	0	0	0	0	0	0	0	0	0	0	0	0	0	0	
1	-4	7	-4	1	0	0	0	0	0	0	0	0	0	0	0	0	0	0	0	0	0	
2	1	-4	6	-4	1	0	0	0	0	0	0	0	0	0	0	0	0	0	0	0	0	
3	0	1	-4	6	-4	1	0	0	0	0	0	0	0	0	0	0	0	0	0	0	0	
4	0	0	1	-4	6	-4	1	0	0	0	0	0	0	0	0	0	0	0	0	0	0	
5	0	0	0	1	-4	6	-4	1	0	0	0	0	0	0	0	0	0	0	0	0	0	
6	0	0	0	0	1	-4	6	-4	1	0	0	0	0	0	0	0	0	0	0	0	0	
7	0	0	0	0	0	1	-4	6	-4	1	0	0	0	0	0	0	0	0	0	0	0	
8	0	0	0	0	0	0	1	-4	6	-4	1	0	0	0	0	0	0	0	0	0	0	
9	0	0	0	0	0	0	0	1	-4	5,11111	-2,22222	0,11111	0	0	0	0	0	0	0	0	0	
10	0	0	0	0	0	0	0	0	1	-2,22222	1,50327	-0,33987	0,0588235	0	0	0	0	0	0	0	0	
11	0	0	0	0	0	0	0	0	0	0,11111	-0,33987	0,40523	-0,235294	0,0588235	0	0	0	0	0	0	0	
12	0	0	0	0	0	0	0	0	0	0	0,0588235	-0,235294	0,3529412	-0,235294	0,0588235	0	0	0	0	0	0	
13	0	0	0	0	0	0	0	0	0	0	0	0,0588235	-0,235294	0,3529412	-0,235294	0,0588235	0	0	0	0	0	
14	0	0	0	0	0	0	0	0	0	0	0	0	0,0588235	-0,235294	0,3529412	-0,235294	0,0588235	0	0	0	0	
15	0	0	0	0	0	0	0	0	0	0	0	0	0	0,0588235	-0,235294	0,3529412	-0,235294	0,0588235	0	0	0	
16	0	0	0	0	0	0	0	0	0	0	0	0	0	0	0,0588235	-0,235294	0,3529412	-0,235294	0,0588235	0	0	
17	0	0	0	0	0	0	0	0	0	0	0	0	0	0	0	0,0588235	-0,235294	0,3529412	-0,235294	0,0588235	0	
18	0	0	0	0	0	0	0	0	0	0	0	0	0	0	0	0	0,0588235	-0,235294	0,35294118	-0,235294	0,0588235	
19	0	0	0	0	0	0	0	0	0	0	0	0	0	0	0	0	0	0,0588235	-0,235294	0,2941176	-0,235294	
20	0	0	0	0	0	0	0	0	0	0	0	0	0	0	0	0	0	0	0	0	1	
	-2,0000	4,0000	-1,0000	0,0000	0,0000	0,0000	0,0000	0,0000	0,0000	0,0000	0,0000	0,0000	0,0000	0,0000	0,0000	0,0000	0,0000	0,0000	0,0000	-0,0588	0,1176	0,8235

Figure 3.5 Matrix A for the case $\alpha = 0,5$ and $n = 17$, see Section 3.2.

The moment distribution using Eq. (3.2-11) is shown in Figure 3.6 for the same case as in Figure 3.5.

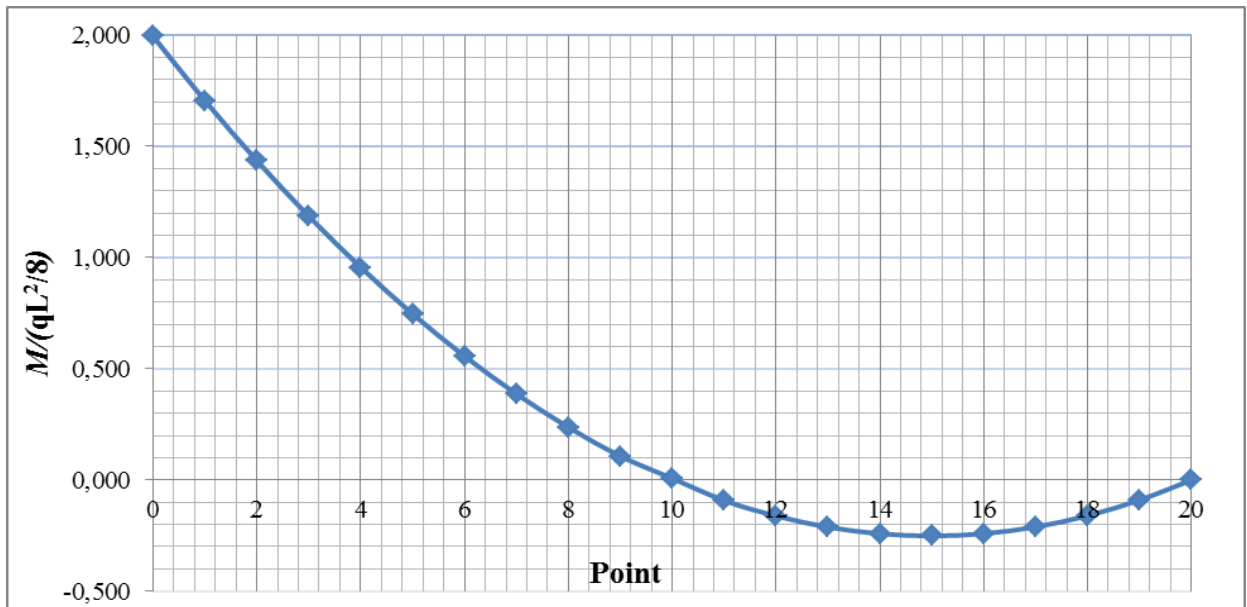


Figure 3.6 Moment variation from A to B for the case $\alpha = 0,5$ and $n = 17$. Observe that the moment at point 10 ($\alpha L = 0,5$) is almost but not exact 0,00. The moment at A is given in Table 3.4. (The numerical method used in Section 3,2 will not give the exact values, but good enough for practical use.)

4. Notations

Roman letter	Definition	Basic unit
D	denominator	-
E	modulus of elasticity	N/m^2
h	parameter	-
I	second moment of area	m^4
I_0	second moment of area at point B	Nm
j, k	numbering of points along the beam from 0 to k	-
L	beam length	m
M	moment	Nm
m	numbering of points at stepped beam stiffness	-
M_A	hogging moment at point A	Nm
n	factor increasing the beam stiffness end at point A	-
N	nominator	-
q	distributed load	N/m
R_B	shear force at point B	N
x	horizontal coordinate	m
y	vertical deflection	m
z	length coordinate	m

Greek letter	Definition	Unit
α	value αL ($0 < \alpha < 1$) defining point of stepped beam stiffness	-
β	factor showing the end hogging moment	-
κ	parameter for defining form of second	
λ	step defining equidistance between points along the beam	
θ	slope deflection	

5. References

Ostenfeld, A, "Teknisk Statik I, 1908

Forssell, G, "Byggnadsstatik I – II, 1919

Timoshenko, & Young, D H, "Theory of Structures", 1945

Nylander, H, "Byggnadsstatik II", 1952

Överblivet material:

$n =$	10	17	100	1 000	10 000	100 000	1 000 000
alfa							
0,000	1,00	1,00	1,00	1,00	1,00	1,00	1,00
0,050	1,13	1,14	1,15	1,15	1,15	1,15	1,15
0,100	1,26	1,28	1,30	1,30	1,30	1,30	1,30
0,150	1,38	1,41	1,44	1,45	1,45	1,45	1,45
0,200	1,49	1,53	1,59	1,60	1,60	1,60	1,60
0,250	1,59	1,65	1,73	1,75	1,75	1,75	1,75
0,300	1,68	1,76	1,87	1,90	1,90	1,90	1,90
0,350	1,75	1,86	2,01	2,05	2,05	2,05	2,05
0,400	1,79	1,93	2,15	2,19	2,20	2,20	2,20
0,450	1,81	1,98	2,27	2,34	2,35	2,35	2,35
0,500	1,79	2,00	2,39	2,49	2,50	2,50	2,50
0,550	1,74	1,98	2,49	2,63	2,65	2,65	2,65
0,600	1,66	1,91	2,55	2,77	2,80	2,80	2,80
0,650	1,54	1,79	2,58	2,91	2,95	2,95	2,95
0,700	1,41	1,63	2,53	3,02	3,09	3,10	3,10
0,750	1,28	1,45	2,37	3,11	3,24	3,25	3,25
0,800	1,16	1,27	2,06	3,13	3,37	3,40	3,40
0,850	1,08	1,13	1,64	2,97	3,48	3,54	3,55
0,900	1,02	1,04	1,24	2,35	3,45	3,67	3,70
0,950	1,00	1,01	1,03	1,32	2,58	3,64	3,83
0,960	1,00	1,00	1,02	1,17	2,12	3,49	3,84
0,970	1,00	1,00	1,01	1,08	1,62	3,12	3,81
0,980	1,00	1,00	1,00	1,02	1,22	2,31	3,61
0,990	1,00	1,00	1,00	1,00	1,03	1,27	2,48
1,000	1,00	1,00	1,00	1,00	1,00	1,00	1,00

Table 3.1 β -values as function of n and α . Points coloured yellow are “close” to the maximum value. Again, $M(x)$ is a second order distribution. Note that $M(\alpha L) = 0$

DANSK SELSKAB FOR BYGNINGSSTATIK

Anmodning om optagelse i selskabet indsendes til et af bestyrelsens medlemmer:

Uffe Graaskov Ravn, Formand
COWI. Mail: ugj@cowi.com

Kåre Flindt Jørgensen, Næstformand
NCC Danmark. Mail: karjor@ncc.dk

Kirsten Riis, Sekretær
Vejdirektoratet. Mail: kiri@vd.dk

Mikkel Christiansen, Kasserer
AB Clausen. Mail: dsby.mc@gmail.com

Andreas Bollerslev, Bestyrelsesmedlem
Niras. Mail: anbo@niras.dk

Jesper Miller Andersen, Bestyrelsesmedlem
VITA ingeniører. Mail: jma@vitaing.dk

Rune Brinker, Bestyrelsesmedlem
Danmarks Tekniske Universitet. Mail: runeb@byg.dtu

Gunnar Ove Bardtrum, Bestyrelsesmedlem
BaneDanmark. Mail: goba@bane.dk

Selskabets formål er at arbejde for den videnskabelige udvikling af bygningsmekanikken - både teori for og konstruktion af alle slags bærende konstruktioner - fremme interessen for faget, virke for et kollegialt forhold mellem dets udøvere og hævde dets betydning overfor og i samarbejde med andre grene af ingeniørvidenskaben. Formålet søges bl.a. realiseret gennem møder med foredrag og diskussioner samt gennem udgivelse af "Bygningsstatiske Meddelelser".

Som medlemmer kan optages personlige medlemmer, firmaer og institutioner, som er særligt interesserede i bygningsmekanik, eller hvis virksomhed falder indenfor bygnings-mekanikkens område.